1D/3D Finite-Volume coupling in conjunction with beam/shell elements coupling for fast transients in pipelines with fluid–structure interaction

Frédéric Daude, P. Galon, T. Douillet-Grellier

Version of Record: https://www.sciencedirect.com/science/article/pii/S0889974621000025
Manuscript_4ad31840f0941e5099a9245acb81df0a

1D/3D Finite-Volume coupling in conjunction with beam/shell elements coupling for fast transients in pipelines with fluid-structure interaction

F. Daude[a,b], P. Galon[a,c], T. Douillet-Grellier[a,b]

[a] *IMSIA, UMR EDF-CNRS-CEA-ENSTA 9219, Université Paris-Saclay, F-91762 Palaiseau, France*
[b] *EDF R&D, ERMES, F-91120 Palaiseau, France*
[c] *CEA Saclay, DEN/SEMT, Université Paris-Saclay, F-91191 Gif-sur-Yvette, France*

Abstract

A 1D/3D Finite-Volume coupling is proposed for the Euler/Homogeneous Equilibrium Model equations. The present approach is based on the Finite-Volume framework making it possible to tackle general equations of state. A special attention is given to the conservation of mass, momentum and energy at the common 1D/3D interface. For fluid-structure interaction induced by fast-transient phenomena occurring in pipelines, the present 1D/3D fluid coupling is also associated with a beam/shell elements coupling to deal with the mechanical pipe behavior. A series of test-cases involving both purely fluid, purely structural and coupled fluid-structure problems with available analytical or experimental references is considered to demonstrate the performance of the present 1D/3D coupling.

Keywords: 1D-3D coupling; Finite-Volume method; Beam/shell elements coupling; Euler/HEM equations; shock-waves

1. Introduction

Pressure waves occurring in piping systems are known to potentially damage pipes or supports affecting directly the operability and the safety of industrial plants. As a consequence, these phenomena have been largely studied using both experiments and numerical simulations [1]. A well-known example of this kind of fluid transients is the water-hammer phenomenon [2]. The numerical approaches encountered in the literature and used for the simulation of such events are mainly one-dimensional and based upon the planar fluid pressure wave propagation assumption. In order to estimate the mechanical consequences on pipes and supports in the computations, fluid-structure interaction (FSI) mechanisms have to be taken into account. For this purpose, two-way coupled approaches where both fluid and pipe motions are tackled simultaneously are considered. In this way, Euler-Bernoulli or Timoshenko beam theory is used for the lateral and torsional pipe motions. As reviewed in [3–6], numerous 1D FSI models have been proposed, ranging from the two-degree-of-freedom (DOF) FSI model (considering the axial motion of both fluid and pipe) to the 7-DOF FSI model (considering one DOF for the fluid plus 6 DOF for the pipe: the axial, the two lateral, the two flexural and the torsional pipe motions while the radial inertia is ignored). All of the previously mentioned FSI models are based on 1D isothermal or isentropic fluid, on low-Mach number flow assumptions and on a linear elastic behavior for the pipe which leads to a linear hyperbolic set of equations. Due to the large size of piping systems in industrial configurations, 1D approaches are widely used and offer a good compromise in terms of computational effort and accuracy. Recently, a non-linear extension of the 1D 7-DOF FSI model have been proposed in [7, 8]. This non-linear modeling is based on the homogeneous equilibrium model (HEM) making it possible to consider the non-linear convective effects which are significant for low wave speeds due to vapor and free gas and to take into account the non-isothermal fluid behavior. In addition, inelastic behavior of the pipe is also considered taking into account material and geometric non-linearities due to elasto-plastic behavior and large pipe displacements.

However, when complex flow phenomena appear which requires to address multi-dimensional flow patterns, the planar wave assumption is not valid anymore. This is the case when fluid flows through elbows, abrupt changes of

Email address: frederic.daude@edf.fr (F. Daude)

pipe cross-section, junctions of several branches or other hydraulic devices inducing significant changes of the flow direction. Thus, the use of 3D approaches is necessary for the required high level of detail as 1D approaches are not adequate to capture the non-planar fluid dynamics wave motion in complex geometry systems. Furthermore, concerning the structural dynamics, due to the limitations of the beam theory assumptions, the 1D approaches are unsuitable to represent the changes in the pipe cross-section as those observed during pipe crushing initiated by impacts for example. In contrast, advanced 3D methods can resolve the details of the flow and the pipe wall in both time and space as in [9]. In this kind of approach, the fluid is modeled using a three-dimensional mathematical model while the pipe is modeled using shell (or solid) elements leading to a high accuracy of the relevant physics in both fluid and structure. However, these methods are CPU and memory costly and, thus, can not be considered for complex piping systems as those involved in industrial plants. In order to combine the efficiency of 1D approaches and the high level of detail obtained with 3D approaches while strongly reducing the CPU time of 3D methodologies, local two-way 1D/3D coupling can be considered. This makes it possible to maintain the accuracy of the obtained numerical results in the case where 3D modeling is only used in the locations where the non-planar flow motion and/or details in the pipe behavior are of interest during the event.

Several approaches have been proposed in order to combine the *reduced* one-dimensional and the *detailed* three-dimensional fluid models. In the literature, most approaches are based on the exchange of variables (mainly pressure and velocity for barotropic flows) between 1D and 3D domains at the common interface. As a consequence, the conservativity of conservative flow variables, i.e. mass, momentum and total energy, through the interface is not guaranteed which is known to be mandatory for shock-wave propagation [10, 11]. Following the works of Hérard & Hurisse [12], Deininger *et al.* [13] have considered the solution of a Riemann problem between two heterogeneous models at the 1D/3D interface by introducing an additional (and discontinuous) variable making it possible to distinguish the one- and the three-dimensional domains. Then, as their 1D/3D interface is artificial, the authors compute the flux for the 1D domain differently from the flux of the 3D domain leading to a loss of conservativity. Wang *et al.* [14] have coupled a 1D water-hammer code with a 3D barotropic CFD code using characteristic equations and Riemann invariants which depend on the considered equation of state. Montenegro *et al.* [15] have coupled a one-dimensional code with a three-dimensional code based on Euler equations in conjunction with a perfect gas equation of state using the same flux at the 1D/3D interface. Bellamoli *et al.* [16] couple 1D and 2D domains in the same code through the flux at the common interface for the junction of several branches and its vicinity in the framework of shallow water flows. This makes it possible to ensure the conservation of mass and momentum in this context at the same time as dealing with transcritical and supercritical flows. In addition, this procedure is non-iterative which is computationally efficient. Due to the high flexibility of the coupling proposed by Bellamoli and co-authors, we will thus follow the ideas proposed in [16] and extend the application to the Euler/HEM equations in conjunction with general equations of state. Furthermore, considering the structural dynamics, two main categories of approaches can be found in the literature to couple elements having different DOF as it is the case of beam and shell elements considered here for tubular structures. The first one is based on the use of transition elements. According to Ho *et al.* [17], many works on the transition elements have been done on shell/solid transitions with very limited work on beam/solid and beam/shell connections. In addition, transition elements are often prone to locking. To try to avoid this problem, reduced integration can be used which leads to the introduction of hourglass modes. Due to these limitations, the transition elements have not been widely used [17]. Thus, we will consider the second category of elements coupling which consists in imposing constraint equations. These constraint equations are here applied to DOF at the nodes constituting the coupling interface between a beam and a shell element. Multi-point constraints (MPC) enforce a relationship between two or more DOF in contrast to single-point constraints. Transformation equations, penalty functions and Lagrange multipliers are the three main methods encountered in the literature that are used to impose MPC equations as explained in [17]. Among the various approaches which can be used, the Lagrange multiplier method makes it possible to ensure a high precision. For this reason, this approach has been retained and previously adapted in order to fit into the explicit integration scheme [18]. In addition, no arbitrary parameter is allowed for ensuring the constraints in contrast to penalty methods. The treatment of essential boundary conditions and MPC equations, that are in both cases expressed in the form of kinematic relationships (prescribed displacements or imposed velocities) of the relevant DOF, is thus tackled using the Lagrange multiplier method.

The paper is organized as follows. Sect. 2 is dedicated to the present 3D approach where fluid is modeled using three-dimensional HEM/Euler equations coupled with the pipe modeled by shell elements. The Finite-Volume method used for the approximation of the fluid dynamics is briefly recalled in the Arbitrary Lagrangian-Eulerian framework

as well as the updated Lagrangian Finite-Element approach used for the pipe. The weak fluid-structure coupling used here, i.e. fluid and structural equations are solved independently and fluid-structure interface conditions are not enforced at each time step, is also described. Then, in Sect. 3, the reduced 1D FSI model previously proposed in [7, 8] is briefly recalled as well as the associated numerical methods. Afterwards, Sect. 4 is devoted to the 1D/3D fluid coupling as well as the beam/shell elements coupling. In Sect. 5, the present approach is then assessed on several test-cases. Finally, the paper ends with a conclusion in Sect. 6.

2. The 3D FSI model and its coupled Finite-Volume/Finite-Element numerical approximation

In the next two sections, the models used to describe the fluid and the structure dynamics as well as their interaction are described: first the 3D fluid-structure interaction modeling and then the 1D reduced FSI model. In both cases, governing equations describing fluid and structure motions and the coupling conditions are detailed along with the corresponding numerical approximations.

2.1. Governing equations

2.1.1. Governing equations for the fluid

The propagation of pressure waves in compressible flows can be modeled with good accuracy with the inviscid Euler equations. The present study is thus restricted to compressible inviscid flows described using the classical 3D Euler equations composed of the mass, momentum and total energy non-linear conservation laws in the fluid domain denoted by Ω_f:

$$\left\{\begin{array}{lcll} \partial_t \rho_\mathrm{f} & + & \nabla\cdot(\rho_\mathrm{f}\boldsymbol{u}_\mathrm{f}) & = 0 \\ \partial_t(\rho_\mathrm{f}\boldsymbol{u}_\mathrm{f}) & + & \nabla\cdot(\rho_\mathrm{f}\boldsymbol{u}_\mathrm{f}\otimes\boldsymbol{u}_\mathrm{f} + p\boldsymbol{I_d}) & = \boldsymbol{0} \\ \partial_t(\rho_\mathrm{f} e_\mathrm{f}) & + & \nabla\cdot(\rho_\mathrm{f} e_\mathrm{f}\boldsymbol{u}_\mathrm{f} + p\boldsymbol{u}_\mathrm{f}) & = 0 \end{array}\right. \tag{2.1}$$

ρ_f, $\boldsymbol{u}_\mathrm{f}$, p and e_f are respectively the fluid density, velocity vector, pressure and specific total energy, $\boldsymbol{I_d}$ is the identity tensor. The subscript f denotes fluid variables and is used whenever a distinction between fluid and structure is necessary. The specific internal energy ε_f is given by $\varepsilon_\mathrm{f} = e_\mathrm{f} - \boldsymbol{u}_\mathrm{f}^2/2$. Eqs. (2.1) are completed by the addition of an equation of state (EOS) giving the specific internal energy ε_f as a function of pressure p and density ρ_f. In the present work, two EOS are considered. The first one is the ideal perfect gas EOS with $p = \rho_\mathrm{f}(\gamma-1)\varepsilon_\mathrm{f}$ where γ is the ratio of specific heats. Finally, to represent steam-water flows, the Steam Tables based on the 1984 NBS/NRC (National Bureau of Standards/National Research Council of Canada) [19] are here used as it was done previously in [7, 8, 20, 21]. Thanks to the use of EOS, other thermodynamical variables can be obtained as a function of pressure and density such as temperature T_f and speed of sound c_f. System in Eq. (2.1) is hyperbolic and the corresponding eigenvalues are in 1D: $\lambda_1 = u_\mathrm{f} - c_\mathrm{f}$, $\lambda_2 = u_\mathrm{f}$ and $\lambda_3 = u_\mathrm{f} + c_\mathrm{f}$. The field associated with eigenvalue λ_2 is linearly degenerate (LD), other fields are genuinely non-linear (GNL).

2.1.2. Governing equations for the structure

The dynamics of the structure is given by the following linear momentum equation describing the equilibrium between inertial, internal and external forces in the structural domain Ω_s:

$$\rho_\mathrm{s}\ddot{\boldsymbol{d}} - \nabla\cdot\boldsymbol{\sigma} = \boldsymbol{f} \tag{2.2}$$

where ρ_s is the structural material density, $\boldsymbol{d}$ the displacement vector, $\ddot{\boldsymbol{d}}$ the acceleration vector, $\boldsymbol{\sigma}$ the Cauchy stress tensor and $\boldsymbol{f}$ the external body forces vector. Note that in Eq. (2.2), the superposed dot denotes the material (or total) time derivative while the divergence operator denotes derivatives with respect to the Eulerian (or spatial) coordinates. In order to determine $\boldsymbol{\sigma}$ the Cauchy stress tensor, various constitutive laws can be used (elastic, elasto-plastic,...). For example in the case of solid elements, the constitutive law corresponding to isotropic linear elastic materials can be written as:

$$\boldsymbol{\sigma} = 2\mu_\mathrm{s}\boldsymbol{\epsilon} + \lambda_\mathrm{s}\mathrm{trac}(\boldsymbol{\epsilon})\boldsymbol{I_d} \quad \text{with} \quad \boldsymbol{\epsilon} = \frac{1}{2}\left(\nabla\boldsymbol{d} + (\nabla\boldsymbol{d})^t - (\nabla\boldsymbol{d})^t\nabla\boldsymbol{d}\right)$$

where $\boldsymbol{\epsilon}$ is the Almansi strain tensor, λ_s and μ_s are the Lamé coefficients, related to the two formulae:

$$\lambda_\mathrm{s} = \frac{E\nu_\mathrm{P}}{(1+\nu_\mathrm{P})(1-2\nu_\mathrm{P})} \quad \text{and} \quad \mu_\mathrm{s} = \frac{E}{2(1+\nu_\mathrm{P})}$$

with E the Young's modulus and ν_P the Poisson's ratio.

On the boundary of the structural domain $\partial\Omega_\mathrm{s}$, additional boundary conditions have to be satisfied. Assuming that the boundary of the structural domain is decomposed in two distinct parts:

$$\partial\Omega_\mathrm{s} = \partial\Omega_{\mathrm{s},d} \cup \partial\Omega_{\mathrm{s},t} \tag{2.3}$$

where the displacements are prescribed on $\partial\Omega_{\mathrm{s},d}$ whereas the traction is prescribed on $\partial\Omega_{\mathrm{s},t}$. The following boundary conditions are thus considered:

$$\begin{cases} \boldsymbol{\sigma}\cdot\boldsymbol{n} = \overline{\boldsymbol{t}} & \text{on } \partial\Omega_{\mathrm{s},t} \\ \boldsymbol{d} = \overline{\boldsymbol{d}} & \text{on } \partial\Omega_{\mathrm{s},d} \end{cases} \tag{2.4}$$

where $\overline{\boldsymbol{d}}$ and $\overline{\boldsymbol{t}}$ are the (prescribed) boundary surface displacement and traction, respectively.

2.1.3. Fluid-Structure coupling conditions

The coupling between the fluid and the structure acts at the common interface between the fluid and the solid domains: $\partial\Omega_\mathrm{f} \cap \partial\Omega_\mathrm{s}$. At this interface, the two following FSI conditions have to be verified for inviscid flows:

$$\begin{cases} \boldsymbol{u}_\mathrm{f}\cdot\boldsymbol{n} = \dot{\boldsymbol{d}}\cdot\boldsymbol{n} & \text{Continuity of the normal velocity} \\ -p\boldsymbol{n} = \boldsymbol{\sigma}\cdot\boldsymbol{n} & \text{Continuity of the stresses normal components} \end{cases} \tag{2.5}$$

where $\boldsymbol{n}$ is a unit normal vector of the interface $\partial\Omega_\mathrm{f} \cap \partial\Omega_\mathrm{s}$. Using Eqs. (2.4) and (2.5), the traction $\overline{\boldsymbol{t}}$ on the common interface between fluid and structure is given by:

$$\overline{\boldsymbol{t}} = -p\boldsymbol{n} \text{ on } \partial\Omega_\mathrm{f} \cap \partial\Omega_\mathrm{s}$$

with p the fluid pressure.

2.2. Numerical methods

The numerical methods used to approximate Eqs. (2.1) and (2.2) are here described. A Finite-Volume method is used for the fluid motion while a Finite-Element approach is considered for structures. In addition, the non-iterative explicit coupling algorithm between these two numerical methods is also presented to show how the coupling between fluid and structure is tackled in the discrete way. Finally, the explicit stability condition is mentioned.

2.2.1. Arbitrary Lagrangian-Eulerian Finite-Volume approximation for the fluid

The explicit cell-centered finite-volume approximation used for the fluid motion is here described for the Arbitrary Lagrangian-Eulerian formulation.

Using the Reynolds transport theorem as well as the Green formula, the unsteady compressible Euler Eqs. (2.1) for any arbitrary closed volume $C(t)$ of boundary $\partial C(t)$ can be expressed in an integral form as:

$$\frac{\mathrm{d}}{\mathrm{d}t}\int_{C(t)} \boldsymbol{U}\mathrm{d}V + \int_{\partial C(t)} \boldsymbol{F}\left(\boldsymbol{U},\boldsymbol{v},\boldsymbol{n}\right)\mathrm{d}S = \boldsymbol{0} \tag{2.6}$$

where $\boldsymbol{v}$ is the velocity of the boundary $\partial C(t)$ and $\boldsymbol{n}$ is the outward unit normal vector on $\partial C(t)$ with respect to $C(t)$. $\boldsymbol{U}$ is the vector of the conserved variables and $\boldsymbol{F}\left(\boldsymbol{U},\boldsymbol{v},\boldsymbol{n}\right)$ is the ALE (Arbitrary Lagrangian-Eulerian) inviscid flux-vector (in the $\boldsymbol{n}$ direction) given by:

$$\boldsymbol{U} = \begin{pmatrix} \rho_\mathrm{f} \\ \rho_\mathrm{f}\boldsymbol{u}_\mathrm{f} \\ \rho_\mathrm{f}e_\mathrm{f} \end{pmatrix} \quad \text{and} \quad \boldsymbol{F} = \begin{pmatrix} \rho_\mathrm{f}\Big(\left(\boldsymbol{u}_\mathrm{f}-\boldsymbol{v}\right)\cdot\boldsymbol{n}\Big) \\ \rho_\mathrm{f}\boldsymbol{u}_\mathrm{f}\Big(\left(\boldsymbol{u}_\mathrm{f}-\boldsymbol{v}\right)\cdot\boldsymbol{n}\Big) + p\boldsymbol{n} \\ \rho_\mathrm{f}e_\mathrm{f}\Big(\left(\boldsymbol{u}_\mathrm{f}-\boldsymbol{v}\right)\cdot\boldsymbol{n}\Big) + p\boldsymbol{u}_\mathrm{f}\cdot\boldsymbol{n} \end{pmatrix}$$

In Eq. (2.6), the choice $\boldsymbol{v} = \boldsymbol{u}_\mathrm{f}$ corresponds to the Lagrangian view of the conservation laws whereas the choice $\boldsymbol{v} = \boldsymbol{0}$ corresponds to the Eulerian counterpart. Because of the generality of the description used in Eq. (2.6), it is referred to as the Arbitrary Lagrangian-Eulerian form of the conservation laws [22].

When moving/deforming grids are considered, the movement of the mesh should not deteriorate the flow field variables. The consideration of Eq. (2.6), written for a constant state, leads to the following relation:

$$\frac{\mathrm{d}}{\mathrm{d}t}\Big(|C\,(t)\,|\Big) - \int_{\partial C(t)} \boldsymbol{v}\cdot\boldsymbol{n}\mathrm{d}S \;=\; 0 \tag{2.7}$$

This relation is purely geometric and links the closed control volume $C\,(t)$, its boundary $\partial C(t)$, the boundary velocity vector $\boldsymbol{v}$ and the unit normal vector $\boldsymbol{n}$. This geometric statement which governs the time rate of change of the volume of $C\,(t)$ is referred to as geometric conservation law (GCL) [23]. The GCL must be satisfied, either explicitly or implicitly, if the conservative property is to be maintained [24].

Using the cell average of the vector of the conserved variables:

$$\boldsymbol{U}_i \equiv \frac{1}{|C_i|}\int_{C_i} \boldsymbol{U}\mathrm{d}V$$

the cell-centered Finite-Volume approximation of Eq. (2.1) on the cell C_i is:

$$\frac{\mathrm{d}}{\mathrm{d}t}\Big(|C_i|\boldsymbol{U}_i\Big) + \sum_{l\in\partial C_i} \boldsymbol{\Phi}_{i,l}A_l = \boldsymbol{0}$$

The numerical flux function $\boldsymbol{\Phi}_{i,l}$ is defined to approximate the surface average of the ALE flux-vector over the cell interface l with respect to cell C_i:

$$\boldsymbol{\Phi}_{i,l}\left(\boldsymbol{U}_L,\boldsymbol{U}_R,\boldsymbol{v}_l,\boldsymbol{n}_{i,l}\right) \approx \frac{1}{A_l}\int_l \boldsymbol{F}\left(\boldsymbol{U},\boldsymbol{v},\boldsymbol{n}_{i,l}\right)\mathrm{d}S$$

with $\boldsymbol{n}_{i,l}$ is the outward normal with respect to cell C_i of cell interface l. $\boldsymbol{U}_L$ and $\boldsymbol{U}_R$ are approximations of the solution on each side of the interface l, left and right respectively and $\boldsymbol{v}_l$ the mesh velocity of the interface l. The numerical flux function $\boldsymbol{\Phi}_{i,l}$ has to satisfy consistency and conservation properties, i.e.

$$\begin{cases} \boldsymbol{\Phi}_{i,l}\left(\boldsymbol{U},\boldsymbol{U},\boldsymbol{v}_l,\boldsymbol{n}_{i,l}\right) = \boldsymbol{F}\left(\boldsymbol{U},\boldsymbol{v}_l,\boldsymbol{n}_{i,l}\right) & \text{Consistency} \\ \boldsymbol{\Phi}_{i,l}\left(\boldsymbol{U}_L,\boldsymbol{U}_R,\boldsymbol{v}_l,\boldsymbol{n}_{i,l}\right) = -\boldsymbol{\Phi}_{i,l}\left(\boldsymbol{U}_R,\boldsymbol{U}_L,\boldsymbol{v}_l,-\boldsymbol{n}_{i,l}\right) & \text{Conservation} \end{cases} \tag{2.8}$$

The numerical flux function used in this paper is based on the HLLC approximate Riemann solver of Toro *et al.* [25–27] written on moving grids as in Luo *et al.* [28]:

$$\boldsymbol{\Phi}_{i,l}^{\mathrm{HLLC}}\left(\boldsymbol{U}_L,\boldsymbol{U}_R,\boldsymbol{v}_l,\boldsymbol{n}_{i,l}\right) \;=\; \begin{cases} \boldsymbol{\Phi}_L & \text{if} \quad 0 < \mathbb{S}_L \\ \boldsymbol{\Phi}_L^* & \text{if} \quad \mathbb{S}_L \le 0 < \mathbb{S}_M \\ \boldsymbol{\Phi}_R^* & \text{if} \quad \mathbb{S}_M \le 0 < \mathbb{S}_R \\ \boldsymbol{\Phi}_R & \text{if} \quad \mathbb{S}_R \le 0 \end{cases} \tag{2.9}$$

where $\boldsymbol{\Phi}_K = \boldsymbol{F}\left(\boldsymbol{U}_K,\boldsymbol{v}_l,\boldsymbol{n}_{i,l}\right)$ with the ALE flux-vector:

$$\boldsymbol{F}\left(\boldsymbol{U}_K,\boldsymbol{v}_l,\boldsymbol{n}_{i,l}\right) = \begin{pmatrix} (\rho_{\mathrm{f}})_K\,\boldsymbol{w}_K\cdot\boldsymbol{n}_{i,l} \\ (\rho_{\mathrm{f}})_K\,(\boldsymbol{u}_{\mathrm{f}})_K\,\boldsymbol{w}_K\cdot\boldsymbol{n}_{i,l} + p_K\boldsymbol{n}_{i,l} \\ (\rho_{\mathrm{f}})_K\,(e_{\mathrm{f}})_K\,\boldsymbol{w}_K\cdot\boldsymbol{n}_{i,l} + p_K\,(\boldsymbol{u}_{\mathrm{f}})_K\cdot\boldsymbol{n}_{i,l} \end{pmatrix}$$

and

$$\boldsymbol{\Phi}_K^* = \frac{1}{\mathbb{S}_K-\mathbb{S}_M}\begin{pmatrix} (\rho_{\mathrm{f}})_K\,(\mathbb{S}_K-\boldsymbol{w}_K\cdot\boldsymbol{n}_{i,l})\,\mathbb{S}_M & & \\ (\rho_{\mathrm{f}})_K\,(\boldsymbol{u}_{\mathrm{f}})_K\,(\mathbb{S}_K-\boldsymbol{w}_K\cdot\boldsymbol{n}_{i,l})\,\mathbb{S}_M & + & p_M\mathbb{S}_K\boldsymbol{n}_{i,l} - p_K\mathbb{S}_M\boldsymbol{n}_{i,l} \\ (\rho_{\mathrm{f}})_K\,(e_{\mathrm{f}})_K\,(\mathbb{S}_K-\boldsymbol{w}_K\cdot\boldsymbol{n}_{i,l})\,\mathbb{S}_M & + & p_M\mathbb{S}_K\mathbb{S}_M - p_K\mathbb{S}_M\,(\boldsymbol{u}_{\mathrm{f}})_K\cdot\boldsymbol{n}_{i,l} + p_M\mathbb{S}_K\boldsymbol{v}_l\cdot\boldsymbol{n}_{i,l} \end{pmatrix}$$

with $K = L, R$, where $\boldsymbol{w}$ is the relative speed given by $\boldsymbol{w} = \boldsymbol{u}_\mathrm{f} - \boldsymbol{v}_l$, the pressure p_M is given by:

$$p_M = (\rho_\mathrm{f})_L \left(\mathbb{S}_L - \boldsymbol{w}_L \cdot \boldsymbol{n}_{i,l}\right)\left(\mathbb{S}_M - \boldsymbol{w}_L \cdot \boldsymbol{n}_{i,l}\right) + p_L = (\rho_\mathrm{f})_R \left(\mathbb{S}_R - \boldsymbol{w}_R \cdot \boldsymbol{n}_{i,l}\right)\left(\mathbb{S}_M - \boldsymbol{w}_R \cdot \boldsymbol{n}_{i,l}\right) + p_R$$

and the speed $\mathbb{S}_M$ defined as:

$$\mathbb{S}_M = \frac{(\rho_\mathrm{f})_R \, \boldsymbol{w}_R \cdot \boldsymbol{n}_{i,l} \left(\mathbb{S}_R - \boldsymbol{w}_R \cdot \boldsymbol{n}_{i,l}\right) - (\rho_\mathrm{f})_L \, \boldsymbol{w}_L \cdot \boldsymbol{n}_{i,l} \left(\mathbb{S}_L - \boldsymbol{w}_L \cdot \boldsymbol{n}_{i,l}\right) + p_L - p_R}{(\rho_\mathrm{f})_R \left(\mathbb{S}_R - \boldsymbol{w}_R \cdot \boldsymbol{n}_{i,l}\right) - (\rho_\mathrm{f})_L \left(\mathbb{S}_L - \boldsymbol{w}_L \cdot \boldsymbol{n}_{i,l}\right)}$$

The speeds $\mathbb{S}_L$ and $\mathbb{S}_R$ corresponding to the fastest waves arising from the solution of the Riemann problem at each side of the interface are computed as proposed in Batten *et al.* [29]:

$$\mathbb{S}_L = \min\left(\boldsymbol{w}_L \cdot \boldsymbol{n}_{i,l} - (c_\mathrm{f})_L \, , \hat{\boldsymbol{w}} \cdot \boldsymbol{n}_{i,l} - \hat{c}_\mathrm{f}\right) \quad \text{and} \quad \mathbb{S}_R = \max\left(\boldsymbol{w}_R \cdot \boldsymbol{n}_{i,l} + (c_\mathrm{f})_R \, , \hat{\boldsymbol{w}} \cdot \boldsymbol{n}_{i,l} + \hat{c}_\mathrm{f}\right)$$

with $\hat{\boldsymbol{w}} = \hat{\boldsymbol{u}}_\mathrm{f} - \boldsymbol{v}_l$ and $\hat{c}_\mathrm{f}$ the Roe average of the velocity $\boldsymbol{u}_\mathrm{f}$ and speed of sound c_f variables.

Using the previous approximations in the ordinary discrete equation (2.6), the integration on the temporal interval $[t^n, t^{n+1}]$ leads to:

$$|C_i^{n+1}| \boldsymbol{U}_i^{n+1} - |C_i^n| \boldsymbol{U}_i^n + \Delta t^n \sum_{l \in \partial \overline{C}_i} \boldsymbol{\Phi}_{i,l} \left(\boldsymbol{U}_L, \boldsymbol{U}_R, \overline{\boldsymbol{v}}_l, \overline{\boldsymbol{n}}_{i,l}\right) A_l = \boldsymbol{0} \tag{2.10}$$

The first-order accuracy in time and in space is obtained using $\boldsymbol{U}_L = \boldsymbol{U}_i^n$ and $\boldsymbol{U}_R = \boldsymbol{U}_{j_l}^n$ with C_{j_l} the adjacent cell of C_i through the interface l: it corresponds to the explicit backward Euler scheme. Second-order accuracy in time and space is achieved using the MUSCL-Hancock approach proposed by van Leer [30] as it was previously described in [31, 32]. The time-step Δt^n in Eq. (2.10) is directly given by a stability condition which will be detailed in Sect. 2.2.4.

Enforcing the GCL at the discrete level is mandatory to the overall numerical conservation property of the scheme in Eq. (2.10). This equation is here verified implicitly via defining the boundary $\partial \overline{C}_i$, the boundary velocity vector $\overline{\boldsymbol{v}}_l$ and the boundary normal vector $\overline{\boldsymbol{n}}_{i,l}$ as a weighted average of their counterpart at the n and $n+1$ time level areas as it was done in [28, 31]. For more details on the GCL and its numerical treatment, the reader can refer to [24, 33–37].

The fluid mesh motion can be arbitrary except on the fluid-solid interface where nodes are common to the fluid and the solid domain and thus have the same motion. The fluid mesh motion can be described by the elastodynamic equations where the fluid mesh is viewed as a pseudo-solid with a linear elastic behavior [33, 38]. Other rezoning algorithms can also be considered [39–41].

2.2.2. Updated Lagrangian Finite-Element approximation for the structure

The explicit time integration used for frames, shells, plates and continua in three dimensions is described below. Both material non-linearities due to elasto-plastic behavior and geometric non-linearities due to large displacements are also considered. The main features of the used algorithm are briefly recalled in the following. For the interested reader, more details can be found in [18].

An updated Lagrangian description is used for the solid domain. In this kind of formulation, the derivatives are with respect to the spatial (Eulerian) coordinates and the weak form involves integrals over the deformed (or current) configuration. The basic discrete equations to be solved are the equilibrium equations which stem from the principle of virtual work expressing the weak form of the conservation of momentum in Eq. (2.2) for the solid domain:

$$\int_{\Omega_\mathrm{s}} \rho_\mathrm{s} \ddot{\boldsymbol{d}} \cdot \delta \boldsymbol{d} \mathrm{d}V = \int_{\Omega_\mathrm{s}} \boldsymbol{f} \cdot \delta \boldsymbol{d} \mathrm{d}V + \int_{\partial \Omega_{\mathrm{s},t}} \overline{\boldsymbol{t}} \cdot \delta \boldsymbol{d} \mathrm{d}S - \int_{\Omega_\mathrm{s}} \boldsymbol{\sigma} : \nabla \delta \boldsymbol{d} \mathrm{d}V \tag{2.11}$$

with $\delta \boldsymbol{d}$ the virtual displacements compatible with the essential boundary conditions, i.e. $\delta \boldsymbol{d} = \boldsymbol{0}$ on $\partial \Omega_{\mathrm{s},d}$.

In the Finite-Element method, the solid domain Ω_s is first divided into elements Ω_e interconnected by nodes. The motion $\boldsymbol{d}^e$, the velocity $\dot{\boldsymbol{d}}^e$ and the acceleration $\ddot{\boldsymbol{d}}^e$ are then approximated within each element using shape functions by:

$$\boldsymbol{d}^e(\boldsymbol{X},t) \approx \sum_{k=1}^{n_e} \psi_k(\boldsymbol{X})\, \boldsymbol{d}_k^e(t), \quad \dot{\boldsymbol{d}}^e(\boldsymbol{X},t) \approx \sum_{k=1}^{n_e} \psi_k(\boldsymbol{X})\, \dot{\boldsymbol{d}}_k^e(t) \quad \text{and} \quad \ddot{\boldsymbol{d}}^e(\boldsymbol{X},t) \approx \sum_{k=1}^{n_e} \psi_k(\boldsymbol{X})\, \ddot{\boldsymbol{d}}_k^e(t)$$

where $\psi_k(\boldsymbol{X})$ are the shape functions, $\boldsymbol{d}_k^e$ is the displacement vector of node k of element e and n_e the nodes number of element e. It can be noticed that the shape functions are expressed in terms of the material coordinates $\boldsymbol{X}$ in the updated Lagrangian formulation even though the weak form is expressed and used in the current configuration. As mentioned in [42], this is essential to reside entirely the time dependence of the finite element approximation in the nodal variables. In addition, the velocity and the acceleration are given by the same shape functions since these functions are constant in time.
As it is not a function of time, the test function and its gradient are approximated in each element as:

$$\delta\boldsymbol{d}^e \approx \sum_{k=1}^{n_e} \psi_k \delta\boldsymbol{d}_k^e \quad \text{and} \quad \nabla\delta\boldsymbol{d}^e \approx \sum_{k=1}^{n_e} \delta\boldsymbol{d}_k^e \otimes \nabla\psi_k$$

where $\delta\boldsymbol{d}_k^e$ are the virtual nodal displacement.
The element nodal variables are related to the system nodal variables by a matrix denoted by $\boldsymbol{L}^e$ termed as *gather* matrix so that:

$$\delta\boldsymbol{d}^e = \boldsymbol{L}^e \delta\boldsymbol{d}$$

Using these approximations in Eq. (2.11) and omitting the sums on the element e and on the nodes i and j for clarity leads to:

$$\left(\int_{\Omega_e} \rho_s \psi_i \psi_j \mathrm{d}V\right) \ddot{\boldsymbol{d}}_j^e \cdot \delta\boldsymbol{d}_i^e = \left(\int_{\Omega_e} \psi_i \boldsymbol{f} \mathrm{d}V\right) \cdot \delta\boldsymbol{d}_i^e + \left(\int_{\partial\Omega_{s,t}\cap\partial\Omega_e} \psi_i \bar{\boldsymbol{t}} \mathrm{d}S\right) \cdot \delta\boldsymbol{d}_i^e - \left(\int_{\Omega_e} \boldsymbol{\sigma}\nabla\psi_i \mathrm{d}V\right) \cdot \delta\boldsymbol{d}_i^e \tag{2.12}$$

As this equality is true for all virtual node displacement $\delta\boldsymbol{d}_i^e$ this gives:

$$\left(\int_{\Omega_e} \rho_s \psi_i \psi_j \mathrm{d}V\right) \ddot{\boldsymbol{d}}_j^e = \int_{\Omega_e} \psi_i \boldsymbol{f} \mathrm{d}V + \int_{\partial\Omega_{s,t}\cap\partial\Omega_e} \psi_i \bar{\boldsymbol{t}} \mathrm{d}S - \int_{\Omega_e} \boldsymbol{\sigma}\nabla\psi_i \mathrm{d}V \tag{2.13}$$

or under the following tensorial form [18]:

$$\mathbf{M}\ddot{\mathbf{d}} = \mathbf{f}_{\text{ext}} - \mathbf{f}_{\text{int}} + \mathbf{f}_c \tag{2.14}$$

with $\mathbf{M}$ the (consistent) mass matrix, $\mathbf{d}$ the nodal discrete displacements, $\ddot{\mathbf{d}}$ the nodal discrete accelerations, $\mathbf{f}_{\text{ext}}$ the external forces, $\mathbf{f}_c$ indicates the vector of unknown reaction forces generated by the essential boundary conditions (see e.g. [18, 43] for more details) and $\mathbf{f}_{\text{int}}$ the internal forces evaluated by spatial integration over the elements:

$$\begin{cases} \mathbf{f}_{\text{ext},i} &= \sum_e \left(\int_{\Omega_e} \psi_i \boldsymbol{f} \mathrm{d}V + \int_{\partial\Omega_{s,t}\cap\partial\Omega_e} \psi_i \bar{\boldsymbol{t}} \mathrm{d}S \right) \\ \mathbf{f}_{\text{int},i} &= \sum_e \left(\int_{\Omega_e} \boldsymbol{\sigma}\nabla\psi_i \mathrm{d}V \right) \end{cases}$$

where the summation symbol represents the assembly operator over all elements e of the FE mesh.

The nodal accelerations $\ddot{\mathbf{d}}$ are obtained from Eq. (2.14) via the inversion of the mass matrix. We recall that the diagonal mass matrix is one of the important features that makes the explicit method efficient and practical [44]. For this reason, the consistent mass matrix is replaced by the lumped mass matrix (reducing to diagonal form) denoted by $\tilde{\mathbf{M}}$ so that the matrix inversion is straightforward.

The set of non-linear second-order ordinary differential equations (ODE) in time given in Eq. (2.14) is approximated with the central difference time integration scheme. Knowing the solution related to the structure at t^n, i.e. the

nodal displacements $\mathbf{d}^n$, velocities $\dot{\mathbf{d}}^n$ and accelerations $\ddot{\mathbf{d}}^n$, the central difference scheme is written as:

$$\begin{cases} \dot{\mathbf{d}}^{n+1/2} = \dot{\mathbf{d}}^n + (\Delta t^n/2)\ddot{\mathbf{d}}^n & (2.15a) \\ \mathbf{d}^{n+1} = \mathbf{d}^n + \Delta t^n \dot{\mathbf{d}}^{n+1/2} & (2.15b) \\ \ddot{\mathbf{d}}^{n+1} = \tilde{\mathbf{M}}^{-1}\left(\mathbf{f}_{\text{ext}}^{n+1} - \mathbf{f}_{\text{int}}^{n+1} + \mathbf{f}_{\text{c}}^{n+1}\right) & (2.15c) \\ \dot{\mathbf{d}}^{n+1} = \dot{\mathbf{d}}^{n+1/2} + (\Delta t^n/2)\ddot{\mathbf{d}}^{n+1} & (2.15d) \end{cases}$$

Note that using two consecutive time steps Δt^{n-1} and Δt^n and after some manipulations, Eq. (2.15) leads to the following relation where the acceleration can be expressed in terms of the displacements:

$$\ddot{\mathbf{d}}^n = \frac{1}{\Delta t^n \Delta t^{n-1/2} \Delta t^{n-1}} \left[\Delta t^{n-1}\left(\mathbf{d}^{n+1} - \mathbf{d}^n\right) - \Delta t^n \left(\mathbf{d}^n - \mathbf{d}^{n-1}\right)\right] \tag{2.16}$$

with $\Delta t^{n-1/2} = \left(\Delta t^n + \Delta t^{n-1}\right)/2$. In the case of equal time steps, this corresponds to the standard central difference formula for the second derivative of a given function. In addition, the central difference scheme corresponds to a particular choice of the Newmark-β time integration with $\gamma = 1/2$ and $\beta = 0$ [42]. This scheme is known to be second-order accurate in time and to introduce no numerical damping [45]. This explicit approach is conditionally stable and has to meet the stability condition on time step size described in Sect. 2.2.4.

Once the updated nodal displacements are known after the second step of the central difference scheme in Eq. (2.15b), the new geometry and the new configuration are known. Knowing the nodal displacement increments $\Delta\mathbf{d} = \mathbf{d}^{n+1} - \mathbf{d}^n$ between two consecutive time steps t^n and t^{n+1} gives the incremental deformation which leads to the increments of strain and then of stress using the constitutive law. Then, the nodal internal forces are updated and then used in Eq. (2.15b) to upgrade the nodal accelerations. Finally, it follows that the nodal velocities are obtained.

2.2.3. Coupled Finite-Volume/Finite-Element approach

The fluid and the structural solvers given in Eq. (2.10) and Eq. (2.15), respectively, are interacting during each time step. For this purpose, the coupling conditions given in Eq. (2.5) should be respected at the discrete level. The main steps of the explicit coupling algorithm are briefly recalled:

1. Knowing the structural solution at time t^n, the nodal velocity is first updated at the mid-step $\dot{\mathbf{d}}^{n+1/2}$ and the nodal displacement at the next time step $\mathbf{d}^{n+1}$ using Eqs. (2.15a) and (2.15b). Then, as it was previously mentioned, the nodal internal forces $\mathbf{f}_{\text{int}}^{n+1}$ are obtained.

2. The known fluid pressure p^n at time t^n at the fluid cells juxtaposing the fluid-structure interface $\partial\Omega_{\text{f}} \cap \partial\Omega_{\text{s}}$ is used for updating the nodal external forces $\mathbf{f}_{\text{ext}}^{n+1}$ with the contribution of the fluid acting at the FSI interface (used in Eq. (2.15c)). This corresponds to the transmission of the traction at the interface due to the fluid pressure loads at the discrete level.

3. The structural solution, i.e. nodal accelerations $\ddot{\mathbf{d}}^{n+1}$ and velocities $\dot{\mathbf{d}}^{n+1}$, is then updated using Eqs. (2.15c) and (2.15d). This corresponds to the time advancement of the structural variables and meshes at time t^{n+1}.

4. The known structural interface velocities $\dot{\mathbf{d}}^{n+1/2}$ at the mid-step are used to compute the mid-step configuration of the fluid-structure interface as $\mathbf{d}^{n+1/2} = \mathbf{d}^n + (\Delta t^n/2)\,\dot{\mathbf{d}}^{n+1/2}$ at $\partial\Omega_{\text{f}} \cap \partial\Omega_{\text{s}}$. These (known) structural interface displacements and velocities are used to update the geometric properties on the fluid mesh. Thus, the mid-step configuration of the fluid grid is obtained in terms of nodal fluid grid velocity $\overline{\mathbf{v}}_f$ and nodal fluid grid displacements:

$$\overline{\mathbf{x}}_f = \mathbf{x}_f^n + \Delta t^n \overline{\mathbf{v}}_f/2$$

which are used to compute the mid-step configuration of geometrical properties associated to edges: boundary of a fluid cell $\partial\overline{C}_i$, interface grid velocity $\overline{v}_l$, interface outward normal $\overline{\boldsymbol{n}}_{i,l}$ (w.r.t. cell $\overline{C}_i$) and surfaces A_l at interface l required for the ALE fluxes in Eq. (2.10). Next, the new or current full-step configuration is updated:

$$\mathbf{x}_f^{n+1} = \overline{\mathbf{x}}_f + \Delta t^n \overline{\mathbf{v}}_f/2$$

used for the evaluation of cell C_i^{n+1}. This step corresponds to the rezoning stage in ALE computations.

5. The fluid variables are thus updated using Eq. (2.10), i.e. the cell-centered conservative variables and then the cell-centered fluid densities $(\rho_\mathrm{f})^{n+1}$, fluid velocities $(\boldsymbol{u}_\mathrm{f})^{n+1}$ and fluid pressures p^{n+1}. This corresponds to the time advancement of the fluid variables at time t^{n+1}.

Note that this time integration scheme is explicit and thus conditionally stable. The corresponding stability condition on time step size is recalled in the next section.

2.2.4. Stability and time step

The explicit time integration given in Eqs. (2.10) for the fluid equations and in Eqs. (2.15) for the structural ones requires a stability condition which can be expressed as:

$$\Delta t^n = C \min\left(\Delta t_\mathrm{f}^n,\ \Delta t_\mathrm{s}^n \right) \tag{2.17}$$

with $0 < C \leq 1$ the Courant number, Δt_f^n and Δt_f^n are the stable time step obtained with the fluid and structural explicit condition at the time t^n. In 1D, these two critical time steps can be expressed as:

$$\Delta t_\mathrm{s}^n = \min_e \left(\frac{|l_e^n|}{|\lambda_{\mathrm{s},e}^n|} \right) \quad \text{and} \quad \Delta t_\mathrm{f}^n = \min_i \left(\frac{|l_i^n|}{|u_i^n| + c_i^n} \right) \tag{2.18}$$

with $|l_i^n|$ and $|l_e^n|$ a characteristic length of the cell C_i and the element e, respectively, and $\lambda_{\mathrm{s},e}^n$ the current structural wave-speed. The stable time step Δt^n is thus re-evaluated at each time step following Eq. (2.17).
For the computations of fast-transient events occurring in water-filled pipelines, the order of magnitude of the cell size is of $10^{-2} - 10^{-3}$ m, the pressure waves speed is of the order of 5000 m.s^{-1} in steel and 1500 m.s^{-1} in water at 20°C and the fluid velocity is about 1 m.s^{-1}. This leads to an order of magnitude of $10^{-6} - 10^{-7}$ s for the time step. Finally, note that, in theory, the fluid grid velocity has to be taken into account in the computation of the stable time step. In other words, the fluid critical time step should be estimated using the fluid relative velocity $w = u - v$ instead of the fluid velocity u in Eq. (2.18). However, in the practical cases mentioned previously, the fluid relative velocity is very low in comparison with the pressure waves speed in the structures. As a consequence, the approximation made in Eq. (2.18) has a very little influence on the size of the stable time step.

3. The 1D reduced FSI model and its Finite-Volume/Finite-Element discretization

The present 1D FSI model was previously described in [8]. Only the main features of the model are recalled in this section. It relies on a two-way FSI coupling between compressible Euler/HEM equations considering varying cross-sections with the Euler-Bernoulli beam equations. This leads to a non-linear seven degree-of-freedom 1D FSI model. The numerical approximation used here is based on an explicit coupled Finite-Volume/Finite-Element approach. For more details on the reduced 1D FSI model and its discretization, the reader can refer to the previous reference.

3.1. Governing equations

In the following, the governing equations for fluid and pipe are described in the local frame of reference denoted by $(\boldsymbol{\xi}, \boldsymbol{\eta}, \boldsymbol{\zeta})$ assigned to each pipe element. The vector $\boldsymbol{\xi}$ corresponds to the local pipe axis while vectors $\boldsymbol{\eta}$ and $\boldsymbol{\zeta}$ are normal to the pipe axis.

The simplified 1D fluid model is classically obtained integrating the 3D Euler/HEM Eqs. (2.1) over each section normal to the pipe axis leading to the following system:

$$\left\{ \begin{array}{lcllcl} \partial_t\left(\rho_\mathrm{f} A_\mathrm{f}\right) & + & \partial_\xi\left(\rho_\mathrm{f} u_\mathrm{f} A_\mathrm{f}\right) & & = & 0 \\ \partial_t\left(\rho_\mathrm{f} u_\mathrm{f} A_\mathrm{f}\right) & + & \partial_\xi\left(\rho_\mathrm{f} u_\mathrm{f}^2 A_\mathrm{f} + p A_\mathrm{f}\right) & - \ p\partial_\xi A_\mathrm{f} & = & 0 \\ \partial_t\left(\rho_\mathrm{f} e_\mathrm{f} A_\mathrm{f}\right) & + & \partial_\xi\left(\rho_\mathrm{f} e_\mathrm{f} u_\mathrm{f} A_\mathrm{f} + p u_\mathrm{f} A_\mathrm{f}\right) & & = & 0 \end{array} \right. \tag{3.1}$$

where ρ_f, u_f, p and e_f are the cross-sectional average of the fluid density, the cross-sectional averaged flow velocity in the pipe direction ξ, the cross-sectional averaged absolute pressure and the cross-sectional averaged specific total energy. A_f is the pipe cross-section and d is the inner diameter such as $A_\mathrm{f} = \pi d^2/4$.

The two EOS previously mentioned for the ideal perfect gas and the steam-water mixture are also used in the 1D reduced fluid model.

The governing equations of the pipe considering axial, lateral, flexural and torsional motions are given in the local frame of reference by:

$$\left\{\begin{array}{lcl} \rho_s A_s \partial_t v_\xi - \partial_\xi F_\xi = 0 \\ (\rho_s A_s + \rho_f A_f)\,\partial_t v_\eta + \partial^2_{\xi^2} M_\zeta = 0 \\ (\rho_s A_s + \rho_f A_f)\,\partial_t v_\zeta + \partial^2_{\xi^2} M_\eta = 0 \\ \rho_s J_s \partial_t \phi_\xi - \partial_\xi M_\xi = 0 \end{array}\right. \tag{3.2}$$

with ρ_s the solid density, A_s the wall cross-section given by $A_s = \pi\left[(d+2\delta)^2 - d^2\right]/4$ where δ is the wall thickness. $v_k = \partial_t d_k$ is the pipe velocity in the k direction ($k = \xi$ for the axial, $k = \eta$ or $k = \zeta$ for the lateral motions) and d_k the displacement in the k direction. $\phi_\xi = \partial_t \theta_\xi$ is the pipe angular velocity. I_s is the area moment of inertia given by: $I_s = \pi\left[(d+2\delta)^4 - d^4\right]/64$ and J_s is the polar moment of inertia: $J_s = 2I_s$ for a cylindrical pipe. F_ξ is the axial force, M_η and M_ζ the two bending moments and M_ξ the torsional moment. For the Euler-Bernoulli beam theory, rotations are related to displacements through the kinematic conditions leading to the two following relations:

$$\theta_\eta = -\partial_\xi d_\zeta \quad \text{and} \quad \theta_\zeta = +\partial_\xi d_\eta \tag{3.3}$$

The set of the structural governing equations is completed by the constitutive relations giving the expression of forces and moments as functions of displacements and rotations:

$$\left\{\begin{array}{lcl} F_\xi = +A_s E \partial_\xi d_\xi \\ M_\eta = -E I_s \partial^2_{\xi^2} d_\zeta \\ M_\zeta = +E I_s \partial^2_{\xi^2} d_\eta \\ M_\xi = +G J_s \partial_\xi \theta_\xi \end{array}\right. \tag{3.4}$$

with E and G the Young's modulus and the shear modulus of the pipe wall material, respectively, i.e. $G = \frac{E}{2(\nu_P+1)}$ where ν_P is the Poisson's ratio of the pipe material. Note that the presence of fluid in the fluid-filled pipe only contributes to the inertia in the lateral directions as an added-mass effect.

As previously described in [8], the fluid and pipe governing equations are coupled together at each time step: the fluid dynamics generates a thermal-hydraulic loading which induces a response of the structure associated to displacements/deformations and velocities. Then, these pipe velocities provide moving boundary conditions for the fluid motion.

3.2. Numerical methods

The numerical method used for approximating Eqs. (3.1) and (3.2) is based on a Finite-Volume approach for the fluid equations coupled with a Finite-Element method for the pipe motion. More details are available in [8].

The quasi 1D Finite-Volume approach used for the fluid motion in piping systems was previously proposed in [7] and is here only briefly recalled. The 1D discrete fluid equations are obtained using the integral form of the 3D equations over a conical control volume leading to:

$$|C_i^{n+1}|\boldsymbol{W}_i^{n+1} - |C_i^n|\boldsymbol{W}_i^n + \Delta t^n\left[\boldsymbol{\Psi}_{i+1/2}\,(A_f)_{i+1/2} - \boldsymbol{\Psi}_{i-1/2}\,(A_f)_{i-1/2}\right] + p_i^n \boldsymbol{R}_i^n = \boldsymbol{0} \tag{3.5}$$

with Δt^n the time step, $\boldsymbol{W}_i$ the cell average of the state vector, $\boldsymbol{\Psi}_{i\pm1/2}$ the 1D inviscid ALE (Arbitrary Lagrangian-Eulerian) numerical fluxes and $\boldsymbol{R}_i^n$ the term linked to the spatial and temporal changes of area given by:

$$\boldsymbol{W} = \begin{pmatrix} \rho_f \\ \rho_f u_f \\ \rho_f e_f \end{pmatrix}, \quad \boldsymbol{\Psi} = \begin{pmatrix} \rho_f\left(u_f - v_\xi\right) \\ \rho_f u_f\left(u_f - v_\xi\right) + p \\ \rho_f e_f\left(u_f - v_\xi\right) + p u_f \end{pmatrix} \quad \text{and} \quad \boldsymbol{R}_i^n = \begin{pmatrix} 0 \\ -\Delta t^n\left[(A_f)_{i+1/2} - (A_f)_{i-1/2}\right] \\ 0 \end{pmatrix}$$

In the 1D ALE fluxes, the grid velocity corresponds exactly to the axial pipe wall velocity v_ξ. Note that the terms associated with the compression and/or stretching of the pipe are also considered. The numerical flux is here obtained using a HLLC-type finite volume solver [7, 25]. This numerical approach was previously used in conjunction with the consideration of the time variation of the cross-sectional area due to pressure for the simulation of water-hammer with column-separation [20].

As in the 3D case, the updated Lagrangian Finite-Element formulation is used for the approximation of the beam governing equations. As described in [8], spatial discretization is achieved through beam finite elements using two Gauss points. A cubic polynomial and a linear shape functions are, respectively, used to approximate the transverse and axial displacements of the beam element with respect to the corotational coordinates system. The equilibrium equation for the pipe reads:

$$\tilde{\mathbf{M}}\ddot{\mathbf{d}} = \mathbf{f}_{\text{ext}} - \mathbf{f}_{\text{int}} + \mathbf{f}_{\text{c}} \tag{3.6}$$

with $\tilde{\mathbf{M}}$ the lumped mass matrix (see [7] for more details), $\mathbf{d}$ the nodal displacement vector, $\dot{\mathbf{d}}$ the nodal velocity vector, $\ddot{\mathbf{d}}$ the nodal acceleration vector, $\mathbf{f}_{\text{ext}}$ and $\mathbf{f}_{\text{int}}$ the external and internal nodal force vectors, respectively, and $\mathbf{f}_{\text{c}}$ the force vector generated by the essential boundary conditions. As previously described, Eq. (3.6) is then solved using the central difference scheme as in Eq. (2.15).

The quasi 1D Finite-Volume method is coupled with the pipe Finite-Element approach at each time step in a similar way as it was previously described for the 3D case. However, the reader looking for additional information can refer to [8] where specific details on the 1D fluid-beam coupling are given.

3.2.1. Stability and time step

As in 3D, the explicit time integration is conditionally stable and requires the use of times steps driven by a stability condition which is similar to the one expressed in 3D considering both fluid and pipe motions. It reads as in Eqs. (2.17) and (2.18). In particular as expressed in [8], the characteristic length $|l_i^n|$ of the fluid cell corresponds to h_i^n the pipe/beam cell/element length while the stable time step associate to the pipe is given by:

$$\Delta t_{\text{s}}^n = \min_i \left(\frac{2}{(\omega_{\text{s}})_i^n} \right)$$

with ω_{s} the maximum eigenvalue of the beam element considering both longitudinal and flexural characteristic time scales:

$$\omega_{\text{s}} = \max \left(2\frac{c_{\text{s}}}{h}, 2\frac{c_{\text{s}}}{h}\sqrt{\frac{\pi^4 I_{\text{s}}}{A_{\text{s}} h^2}} \right)$$

where c_{s} is the longitudinal wave speed in the structure given by:

$$c_{\text{s}} = \sqrt{\frac{E}{\rho_{\text{s}}}}$$

and I_{s} the area moment of inertia. Note that due to the flexural contribution, the stable time step varies with the square of the element length which can lead to small values in the case of short beam elements as previously discussed in [7].

The present FSI 1D model was previously validated against experimental data on fast-transient phenomena in flexible pipelines involving non-isothermal fluid behavior or material and geometric non-linearities due to elasto-plastic behavior, large pipe bending or large pipe displacements [8].

4. 1D/3D fluid Finite-Volume coupling in conjunction with beam/shell elements coupling

Two domains denoted by $\Omega_{3\text{D}}$ and $\Omega_{1\text{D}}$ are now considered where the 3D fluid-structure model is solved in the first domain while the 1D reduced fluid-structure model is solved in the second one. As a consequence, the considered coupling problem between the two models at the connection of the two domains is here presented for both fluids and structures.

4.1. 1D/3D Finite-Volume coupling for the fluids

The present 1D/3D coupling acts at the common interface between the 1D and the 3D fluid computational domains. This interface is associated with one single edge coming from the 1D domain denoted in the following by $i + 1/2$ corresponding to a 1D conic control volume C_i. This interface is also associated with several edges each one coming from the 3D domain linked to a 3D control volume denoted C_j (cf. Fig. 1). The discrete fluid balance equations for

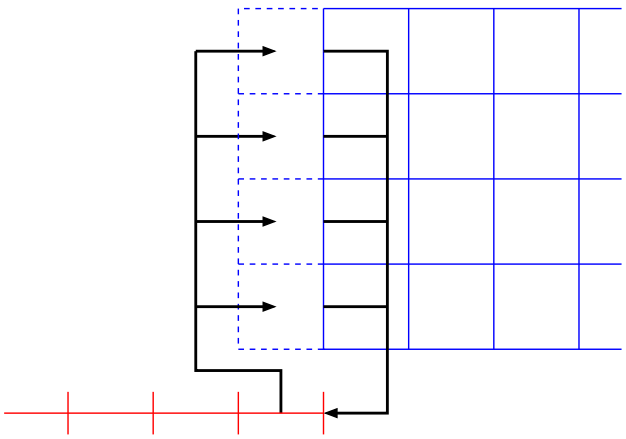

Figure 1: Sketch of the coupling between the 1D domain represented in red and the 3D domain plotted in blue via the common interface.

the cells associated to the common 1D/3D interface can be written as:

$$\begin{cases} |C_j^{n+1}|\boldsymbol{U}_j^{n+1} - |C_j^n|\boldsymbol{U}_j^n + \Delta t^n \sum_l \boldsymbol{\Phi}_{j,l} A_l = \boldsymbol{0} & \text{for all the 3D fluid cells } C_j \\ |C_i^{n+1}|\boldsymbol{W}_i^{n+1} - |C_i^n|\boldsymbol{W}_i^n + \Delta t^n \left[\boldsymbol{\Psi}_{i+1/2}\,(A_{\mathrm{f}})_{i+1/2} - \boldsymbol{\Psi}_{i-1/2}\,(A_{\mathrm{f}})_{i-1/2}\right] + p_i^n \boldsymbol{R}_i^n = \boldsymbol{0} & \text{for the single 1D fluid cell } C_i \end{cases}$$

Thus, the update of the flow variables requires the computation of the 1D numerical flux $\boldsymbol{\Psi}_{i+1/2}$ and all the 3D numerical fluxes $\boldsymbol{\Phi}_{j,l}$ at the edges corresponding to the 1D/3D interface. In the present approach, the computation of these numerical fluxes is based on the solution of the local Riemann problems at all the cell faces constituting the common interface between the 1D and the 3D fluid computational domains. In this way, the conservative variables at the center of the 1D cell connected to the interface are assigned to one of the two states of the local Riemann problems whereas the other state of the local Riemann problems is represented by the conservative variables at the center of each 3D cell having a face associated to the interface between the two domains. Then, the coupling between 1D and 3D domains is achieved via the computation of the 3D flux-vectors based on the local Riemann problems at each cell face previously mentioned. Finally, the 1D flux-vector associated to the 1D/3D interface is computed using conservation principles. As mentioned previously, the 3D numerical fluxes $\boldsymbol{\Phi}_{j,l}$ are a function of a right state, a left state denoted by $\boldsymbol{U}_R$ and $\boldsymbol{U}_L$, respectively, the grid velocity $\boldsymbol{v}_l$ and the unit outward vector $\boldsymbol{n}_{j,l}$ to the associated edge:

$$\boldsymbol{\Phi}_{j,l} = \boldsymbol{\Phi}_{j,l}\left(\boldsymbol{U}_L, \boldsymbol{U}_R, \boldsymbol{v}_l, \boldsymbol{n}_{j,l}\right)$$

The left state $\boldsymbol{U}_L$ is directly obtained using the unknowns linked to the 3D cell C_j, i.e. at the first order in time and space: $\boldsymbol{U}_L = \boldsymbol{U}_j^n$. The unit outward vector $\boldsymbol{n}_{j,l}$ with respect to the 3D domain $\Omega_{3\mathrm{D}}$ corresponds to the unit entering vector w.r.t. the 1D domain $\Omega_{1\mathrm{D}}$, in other words the following relation is respected: $\boldsymbol{n}_{j,l} = -\boldsymbol{n}_{i+1/2}$. In order to compute the 3D numerical flux corresponding to the coupled interface, the right state has to be expressed using the variables coming from the 1D neighboring cell C_i (cf. Fig. 1) such as in first order in time and space:

$$\begin{cases} (\rho_{\mathrm{f}})_R &= (\rho_{\mathrm{f}})_i^n \\ p_R &= p_i^n \\ (\boldsymbol{u}_{\mathrm{f}})_R &= (u_{\mathrm{f}})_i^n\, \boldsymbol{\xi} \end{cases} \tag{4.1}$$

Once all the 3D numerical fluxes $\boldsymbol{\Phi}_{j,l}$ associated with the coupled interface are computed, the 1D flux-vector $\boldsymbol{\Psi}_{i+1/2}$ required to update the conserved variables at the 1D cell connected to the 1D/3D interface is taken as the sum of all the 3D flux-vectors (cf. Fig. 1) previously computed ensuring conservativity between 1D and 3D domains such as:

$$\boldsymbol{\Psi}_{i+1/2}\boldsymbol{\xi}\cdot\boldsymbol{n}_{i+1/2} = -\frac{\beta_{\mathcal{R}}}{(A_{\mathrm{f}})_{i+1/2}}\sum_{l\in\mathcal{R}}\boldsymbol{\Phi}^{\mathrm{1D}}_{j,l}\left(\boldsymbol{U}_L,\boldsymbol{U}_R,\boldsymbol{v}_l,\boldsymbol{n}_{j,l}\right)A_l \quad \text{with} \quad \beta_{\mathcal{R}} = \frac{(A_{\mathrm{f}})_{i+1/2}}{\sum_{l\in\mathcal{R}}A_l} \tag{4.2}$$

with $\boldsymbol{n}_{i+1/2}$ the 3D outward normal vector to cell C_i, $\boldsymbol{U}_L = \boldsymbol{U}^n_j$ and $\boldsymbol{U}_R$ given by Eq. (4.1). $\mathcal{R}$ denotes the set of the edges coming from the 3D domain constituting the 1D/3D interface. $\boldsymbol{\Phi}^{\mathrm{1D}}_{j,l}$ is the 1D projection of the 3D numerical flux $\boldsymbol{\Phi}_{j,l}$ on the pipe axis $\boldsymbol{\xi}$:

$$\boldsymbol{\Phi}^{\mathrm{1D}}_{j,l} = \mathcal{P}_{\boldsymbol{\xi}}\circ\boldsymbol{\Phi}_{j,l}$$

with $\mathcal{P}_{\boldsymbol{\xi}}$ the 1D projection operator on the pipe axis as defined in [7]. This corresponds to the projection of the multi-dimensional component associated to the momentum flux on the pipe axis. Furthermore, the scalar product $\boldsymbol{\xi}\cdot\boldsymbol{n}_{i+1/2}$ in Eq. (4.2) is due to the fact that in 1D discrete balance equations as in Eq. (3.5), the numerical fluxes are naturally linked to the outward normal vector to the corresponding edge.

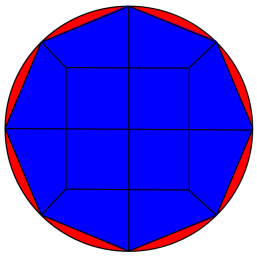

Figure 2: $\beta_{\mathcal{R}}$ is the ratio between the *perfect* circular section $(A_{\mathrm{f}})_{i+1/2}$ issued from the 1D domain Ω_{1D} (here in red) and the discretized surface obtained with the sum of the several edges issued from the 3D domain Ω_{3D} (here in blue).

Finally, the ratio $\beta_{\mathcal{R}}$ is introduced in Eq. (4.2) in order to take into account the potential difference between the *perfect* circular section $(A_{\mathrm{f}})_{i+1/2}$ issued from the 1D domain Ω_{1D} and the discretized surface obtained with the sum of the several edges issued from the 3D domain Ω_{3D} (see Fig. 2). Due to the discretization of the pipe cross-section in the 3D domain, the corresponding cross-section is not a *perfect* circle in the 3D domain in contrast to the 1D domain as it is associated to a diameter. The potential difference between these two cross-sections has no physical meaning and thus should not disturb the fluid motion. In particular, the simple example of a constant solution should be preserved with the present 1D/3D coupling. For this purpose, let us consider in the following a constant state given by constant density, pressure and velocity on fixed grids, i.e. $\rho_{\mathrm{f}} = \overline{\rho}$, $p = \overline{p}$, $u_{\mathrm{f}} = \overline{u}$ and $v_\xi = 0$ in the 1D fluid computational domain and $\rho_{\mathrm{f}} = \overline{\rho}$, $p = \overline{p}$, $\boldsymbol{u}_{\mathrm{f}} = \overline{u}\boldsymbol{\xi}$ and $\boldsymbol{v} = \boldsymbol{0}$ in the 3D fluid computational domain which leads to the following fluxes thanks to the consistency property:

$$\overline{\boldsymbol{\Phi}} = \begin{pmatrix} \overline{\rho}\,\overline{u}\,\boldsymbol{\xi}\cdot\boldsymbol{n} \\ \overline{\rho}\,\overline{u}^2\,\boldsymbol{\xi}\cdot\boldsymbol{n}\,\boldsymbol{\xi} + \overline{p}\boldsymbol{n} \\ \overline{\rho}\,\overline{e}\,\overline{u}\,\boldsymbol{\xi}\cdot\boldsymbol{n} + \overline{p}\,\overline{u}\,\boldsymbol{\xi}\cdot\boldsymbol{n} \end{pmatrix} \quad \text{and} \quad \overline{\boldsymbol{\Psi}} = \begin{pmatrix} \overline{\rho}\,\overline{u} \\ \overline{\rho}\,\overline{u}^2 + \overline{p} \\ \overline{\rho}\,\overline{e}\,\overline{u} + \overline{p}\,\overline{u} \end{pmatrix}$$

for all edges except on the ones associated to the common interface between 1D and 3D domains, with $\overline{e} = \varepsilon(\overline{\rho},\overline{p}) + \overline{u}^2/2$. The fact that all the numerical fluxes are the same at all the cell interfaces makes it possible to preserve the initial steady-state condition. As a consequence, we have to check that the present 1D/3D coupling leads to a preservation of the constant states. At each 3D edges of the common 1D/3D interface, the right state of the corresponding local Riemann problem given in Eq. (4.1) corresponds to the following constant state given by the adjacent 1D cell: $(\rho_{\mathrm{f}})_R = \overline{\rho}$, $(p_{\mathrm{f}})_R = \overline{p}$ and $(\boldsymbol{u}_{\mathrm{f}})_R = \overline{u}\boldsymbol{\xi}$ which leads to the corresponding 3D numerical fluxes $\boldsymbol{\Phi}_{j,l}$ and the corresponding 1D

projections $\mathbf{\Phi}_{j,l}^{\mathrm{1D}}$ on the pipe axis:

$$\mathbf{\Phi}_{j,l} = \begin{pmatrix} \overline{\rho}\,\overline{u}\,\boldsymbol{\xi}\cdot\boldsymbol{n}_{j,l} \\ \overline{\rho}\,\overline{u}^2\,\boldsymbol{\xi}\cdot\boldsymbol{n}_{j,l}\,\boldsymbol{\xi} + \overline{p}\boldsymbol{n}_{j,l} \\ \overline{\rho}\,\overline{e}\,\overline{u}\,\boldsymbol{\xi}\cdot\boldsymbol{n}_{j,l} + \overline{p}\,\overline{u}\,\boldsymbol{\xi}\cdot\boldsymbol{n}_{j,l} \end{pmatrix} = \overline{\mathbf{\Phi}} \quad \text{and} \quad \mathbf{\Phi}_{j,l}^{\mathrm{1D}} = \begin{pmatrix} \overline{\rho}\,\overline{u}\,\boldsymbol{\xi}\cdot\boldsymbol{n}_{j,l} \\ \overline{\rho}\,\overline{u}^2\,\boldsymbol{\xi}\cdot\boldsymbol{n}_{j,l} + \overline{p}\boldsymbol{\xi}\cdot\boldsymbol{n}_{j,l} \\ \overline{\rho}\,\overline{e}\,\overline{u}\,\boldsymbol{\xi}\cdot\boldsymbol{n}_{j,l} + \overline{p}\,\overline{u}\,\boldsymbol{\xi}\cdot\boldsymbol{n}_{j,l} \end{pmatrix} = \overline{\mathbf{\Psi}}\boldsymbol{\xi}\cdot\boldsymbol{n}_{j,l} = -\overline{\mathbf{\Psi}}\boldsymbol{\xi}\cdot\boldsymbol{n}_{i+1/2}$$

Notice that the unit normal vector of the common interface outward w.r.t. the 3D computational domain $\boldsymbol{n}_{j,l}$ is collinear with $\boldsymbol{\xi}$, i.e. $\boldsymbol{\xi}\cdot\boldsymbol{n}_{j,l}\,(=-\boldsymbol{\xi}\cdot\boldsymbol{n}_{i+1/2}) = \pm 1$. Finally, the 1D numerical flux at the 1D/3D interface given in Eq. (4.2) reads:

$$\mathbf{\Psi}_{i+1/2}\boldsymbol{\xi}\cdot\boldsymbol{n}_{i+1/2} = \frac{\beta_{\mathcal{R}}}{(A_{\mathrm{f}})_{i+1/2}}\sum_{l\in\mathcal{R}}\overline{\mathbf{\Psi}}\boldsymbol{\xi}\cdot\boldsymbol{n}_{i+1/2}A_l \quad \text{or equivalently} \quad \mathbf{\Psi}_{i+1/2} = \overline{\mathbf{\Psi}}$$

Finally, all the 3D edges have the same numerical fluxes, i.e. $\overline{\mathbf{\Phi}}$ as all the 1D edges, i.e. $\overline{\mathbf{\Psi}}$, which ensures the preservation of the initial constant state.

Note that in the general case, two non-zero transverse velocity components can be present in the 3D domain. In the present 1D/3D coupling, the transverse components of the momentum flux are omitted and only the normal momentum component is considered which can deteriorate the momentum balance at the common interface. In other words, 1D motion at this interface has to be verified to ensure the momentum conservation at the interface. That thus implies to place the 1D/3D interface in regions where the flow is nearly one-dimensional.

In addition, note that as soon as the solver used for the computation of the numerical vector-fluxes can deal with general Equations Of State (as it is the case with the HLLC scheme), the present 1D/3D coupling can also tackle general EOS as it will be shown latter.

What is more, the present 1D/3D fluid coupling has been used in [46] for the simulation of a blast wave propagating through a shock-tube and then impacting and damaging aluminium plates.

4.2. Beam/shell kinematics coupling for the structures

Concerning the structural motion of the pipe, the present coupling aims at connecting beam and shell elements together at the common interface composed by one single node denoted by q of the adjacent beam element and the nodes denoted by k of the neighbor shell elements (see Fig. 3). For this purpose, the constraint that the degrees of freedom (DOF) at the coupling interface has to be equivalent between beam and shell is imposed. This ensures compatibility between the two element types. To this end, constraint equations applied to DOF at the coupling interface between beam and shell are here considered. The constraint equations used here are based on purely geometric considerations. The coupling interface is assumed to have a rigid body motion which is consistent with the kinematics assumptions

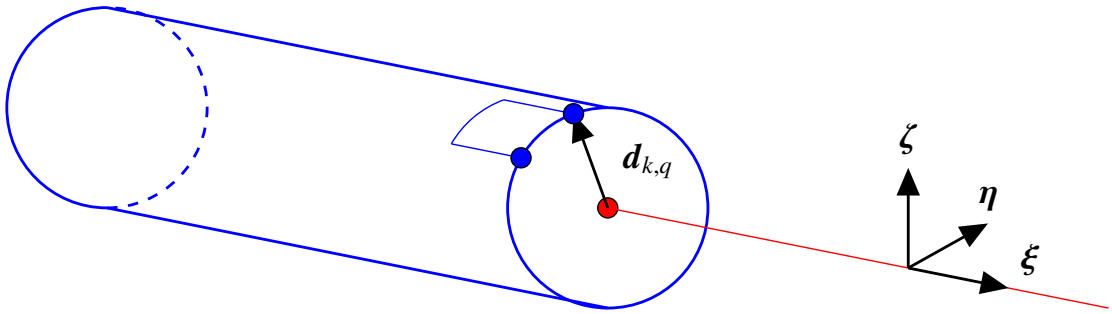

Figure 3: Sketch of the coupling between beam (plotted in red) and shell (plotted in blue) elements using the spatial reference system of orthogonal axis $(\boldsymbol{\xi}, \boldsymbol{\eta}, \boldsymbol{\zeta})$ for the straight pipe element.

for both beam and shell elements. The constraint equations couple the individual translations and rotations of the two

types of elements. The translations on the beam are directly equivalent to those on the shell. Then, to complete the translational DOF on the shell, the effect of the beam rotations is considered. The two following kinematics relations between the single beam node and the several shell nodes corresponding to the common boundary are thus considered:

$$\boldsymbol{\theta}_k^{\text{shell}} = \boldsymbol{\theta}_q^{\text{beam}} \quad \text{with} \quad \boldsymbol{\theta} = \theta_\xi \boldsymbol{\xi} + \theta_\eta \boldsymbol{\eta} + \theta_\zeta \boldsymbol{\zeta} \tag{4.3}$$

where $\boldsymbol{\theta}_k^{\text{shell}}$ (respectively $\boldsymbol{\theta}_q^{\text{beam}}$) corresponds to the rotation vector of the node k of the shell element (respectively of the node q of the beam element) and for each node k of the shell elements constituting the interface its velocity $\boldsymbol{v}_k^{\text{shell}}$ is related to the node velocity $\boldsymbol{v}_q^{\text{beam}}$ of the beam element:

$$\boldsymbol{v}_k^{\text{shell}} = \boldsymbol{v}_q^{\text{beam}} + \boldsymbol{\phi}_q^{\text{beam}} \wedge \boldsymbol{d}_{k,q} \quad \text{with} \quad \boldsymbol{\phi}_q^{\text{beam}} = \partial_t \boldsymbol{\theta}_q^{\text{beam}} \quad \text{and} \quad \boldsymbol{d}_{k,q} = \boldsymbol{x}_k - \boldsymbol{x}_q \tag{4.4}$$

The first kinematics relation corresponds to the equality of the rotation vectors between all the nodes of the shell elements (denoted by k) and the single node of the beam element (denoted by q) all associated to the common interface while the second one corresponds to the rigid body motion assumption mentioned previously. These kinematic constraints are imposed thanks to the use of Lagrange multipliers [18].

When both 1D and 3D FSI models are considered in the same computation, the time step used for this computation should respect stability conditions issued from both 3D and 1D model given in Sect. 3.2.1 and Sect. 2.2.4. That is why the most restrictive condition is used for the stable time step estimation.

All of the models and algorithms described previously for both 3D FSI and 1D FSI models have been implemented in the fast transient dynamics software for fluids and structures *Europlexus* [41] (`http://www-epx.cea.fr/`) co-owned by the French *Commissariat à l'énergie atomique et aux énergies alternatives* (CEA) and by the European Commission. *Électricité de France* (EDF) is involved as a major partner of the consortium built for *Europlexus* software development.

5. Numerical tests

The goal of this section is to assess the capabilities of the present 1D/3D coupling on a collection of analytical and experimental test-cases. The first three tests are purely fluid problems where analytical solutions are available which are studied to evaluate the 1D/3D fluid Finite-Volume coupling. Then, a bending beam problem with an available analytical solution is considered to assess the beam/shell Finite-Element coupling. Finally, a FSI problem of pipe whipping with available experimental data is considered where both 1D/3D fluid and beam/shell elements structural couplings are involved.

5.1. Shock-tube problems

Three shock-tubes are first considered to assess the conservativity property of the present 1D/3D fluid coupling. In these three tests, the tube is assumed to be rigid so that its diameter plays no role. As a consequence, only the fluid motion is here considered. In addition, the tube is long enough (1 m herein) to avoid unwanted reflections at the boundaries of the computational domain. The initial discontinuity is located at the middle of the fluid-filled tube, i.e. $\xi = 0.5$ m. For the present hybrid 1D/3D computations, the tube is discretized using 3D cells from $\xi = 0$ m (which corresponds to the inlet of the pipe) to $\xi = 0.375$ m, then by 1D cells from $\xi = 0.375$ m to $\xi = 0.6875$ m and finally by 3D cells from $\xi = 0.6875$ m to $\xi = 1$ m (corresponding to the outlet of the pipe) as shown in Fig. 4. The longitudinal length (in the $\boldsymbol{\xi}$ direction) of the cells corresponds to $h = 2.5$ mm. Furthermore, 48 cells are used for the discretization of the pipe cross-section in the 3D regions. Due to this discretization, the ratio between the pipe cross-section considered in the 1D domain and the discretized cross-section issued from the 3D region is about 1.0262. The 1D/3D mesh is thus composed of 125 cells in the 1D part of the computational domain and of 13200 cells in the 3D region. The numerical results obtained with the 1D/3D numerical approach are then compared with the 1D results obtained with similar computational parameters (longitudinal length of cells and time step size) and with the analytical solutions of each shock-tube. Only first-order accurate numerical results are here considered to focus exclusively on the performance of the 1D/3D Finite-Volume coupling.

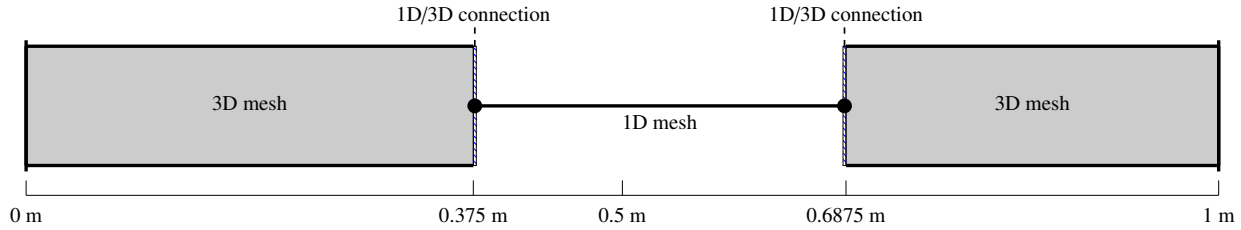

Figure 4: 1D/3D modeling of the shock-tube tests.

5.1.1. Shock-tube in air at rest

In the present shock-tube, the internal diameter of the 1-m long rigid pipe is taken to be equal to $d = 50$ mm which has no influence on the numerical results. The pipe is supposed to be initially separated by a diaphragm in two equal

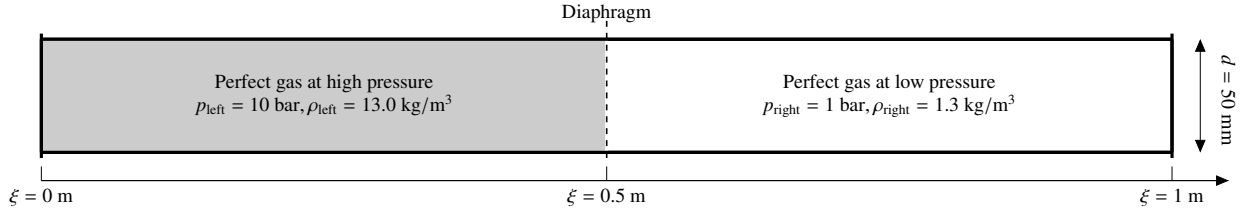

Figure 5: Test description of the shock-tube in air at rest.

parts and closed at both ends as can be seen in Fig. 5. This system is initially at equilibrium. The left part of the tube is filled with a gas at an initial pressure of $p_{\text{left}} = 10$ bar and density of $\rho_{\text{left}} = 13$ kg/m^3. The right part is filled with the same gas, but at an initial pressure of $p_{\text{right}} = 1$ bar and density of $\rho_{\text{right}} = 1.3$ kg/m^3. The fluid is supposed to be a perfect gas with the same temperature in both parts of the tube. The specific heat ratio ($\gamma = C_p/C_v$) is constant and supposed to be equal to 1.4.

At the initial instant, $t_0 = 0$ ms, the diaphragm is opened. The 1D/3D numerical results obtained with a Courant number of $C = 0.9$ (which corresponds to an averaged time step of $\Delta t \approx 3.42$ µs) are then compared to their 1D counterpart and the analytical solutions. The closed ends are reproduced by wall boundary conditions.

The results are presented in Fig. 6 giving the profiles of pressure, velocity and density at $t_f = 0.9$ ms, measured as a function of the abscissa of the tube ($\xi \in [0\text{ m}, 1\text{ m}]$). No discrepancy between the 1D/3D results and the 1D results are observed showing that the present 1D/3D coupling does not introduce any spurious perturbations in the numerical solutions. In addition, the obtained numerical results are in good agreement with the analytical solutions: both shapes and locations of shock and rarefaction waves are correctly predicted while the contact discontinuity is smoothened as expected with the use of first-order accurate schemes.

5.1.2. Shock-tube in pure liquid water at rest

The present test is very similar to the previous one as the same tube is considered but filled by pure liquid water instead of perfect gas as it was done in the previous one (cf. in Fig. 7). The objective here is to demonstrate the ability of the proposed 1D/3D fluid Finite-Volume coupling to deal with general EOS as the 1984 NBS/NRC Steam-Water Tables [19] are here used.

Initially, the left part of the tube is filled with water with an initial pressure of $p_{\text{left}} = 10$ bar, an initial density of $\rho_{\text{left}} = 998.606$ kg/m^3 and an initial speed of sound of $c_{\text{left}} = 1484.49$ m/s. On the other hand, the right part is filled with water, but with an initial pressure of $p_{\text{right}} = 1$ bar, an initial density of $\rho_{\text{right}} = 998.195$ kg/m^3 and an initial speed of sound of $c_{\text{right}} = 1482.83$ m/s. Temperature is supposed to be constant and set to 20°C in both sections of the tube.

At the initial instant, $t_f = 0$ ms, the diaphragm is opened. As previously, the 1D/3D numerical results obtained with a Courant number of $C = 0.75$ corresponding to an averaged time step of $\Delta t \approx 1.26$ µs are compared to their

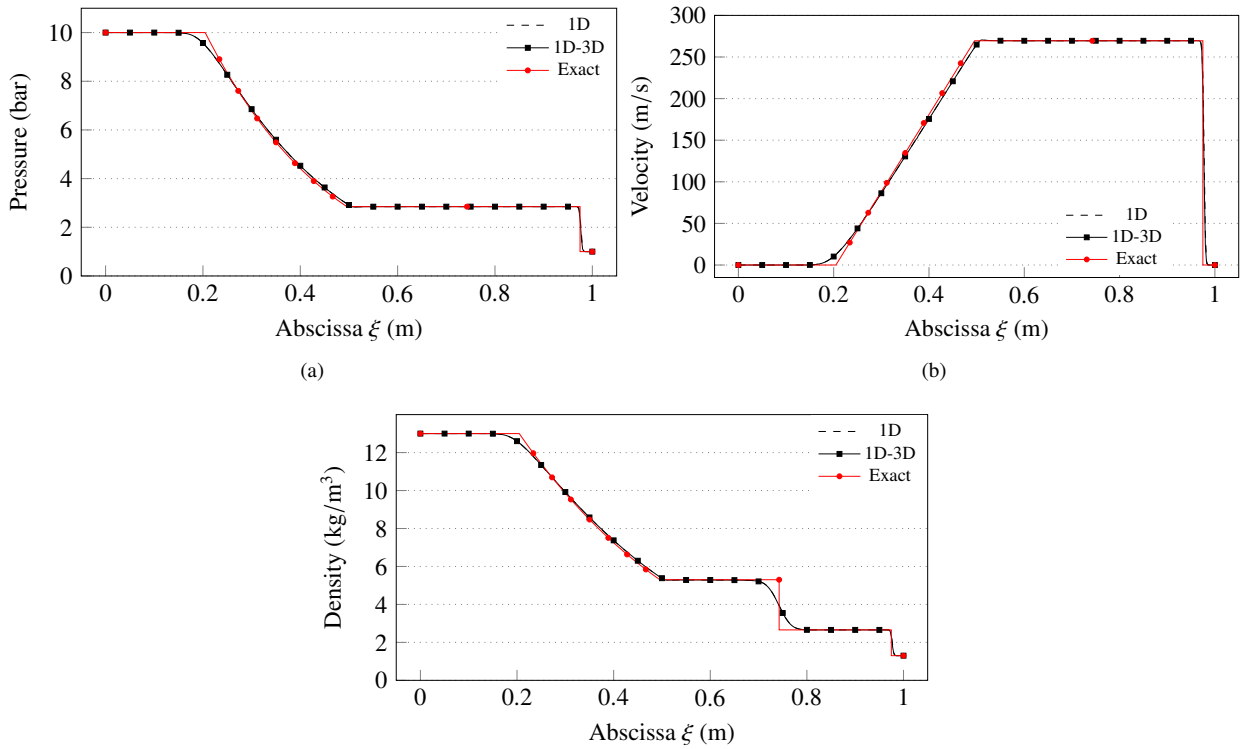

Figure 6: Pressure (a), velocity (b) and density (c) profiles along the tube at $t_f = 0.9$ ms for the shock-tube in air at rest: comparison between the 1D/3D results, the 1D results and the analytical solutions.

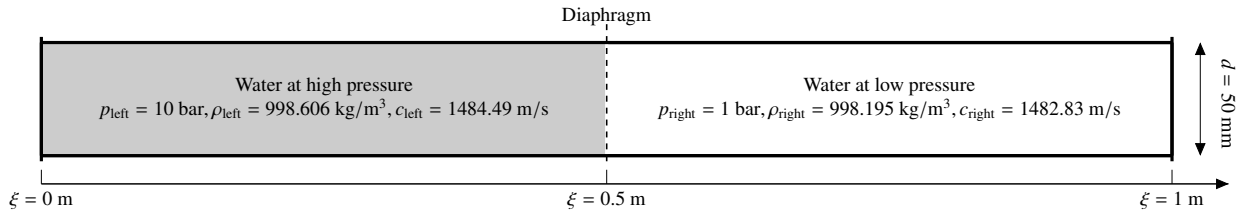

Figure 7: Test description of the shock-tube in pure liquid water at rest.

1D counterpart and the analytical solutions. The closed ends are reproduced by wall boundary conditions as in the previous case.

The analytical solution of the present problem is derived from the Joukowsky theory [47] based on the linearized low-Mach ($u_f \ll c_f$) and isothermal assumptions.

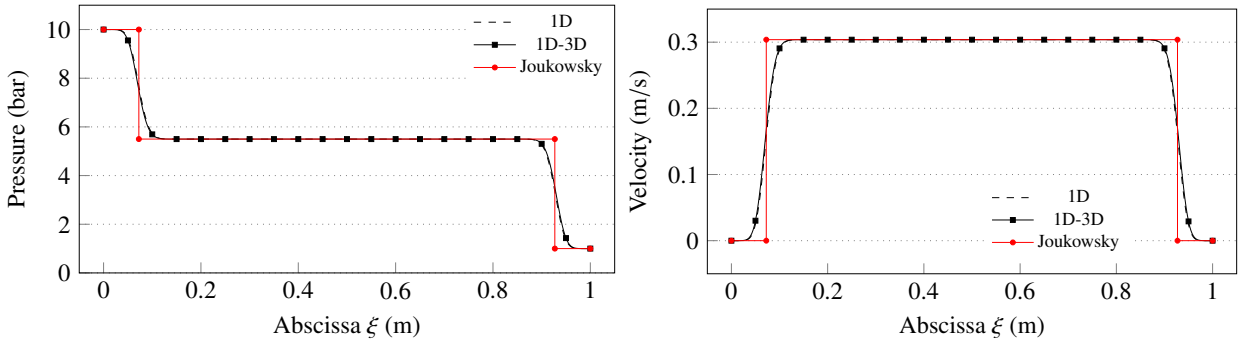

Figure 8: Pressure (a) and velocity (b) profiles along the tube at $t_f = 0.288$ ms for the shock-tube in liquid water at rest: comparison between the 1D/3D results, the 1D results and the analytical solutions.

The results are presented in Fig. 8 showing the profiles of pressure and velocity at $t_f = 0.288$ ms, measured as a function of the abscissa of the tube ($\xi \in [0\text{ m}, 1\text{ m}]$). As previously, no discrepancy between the 1D/3D results and the 1D results are observed. What is more, the obtained numerical results are in good agreement with the analytical solutions: both rarefaction and shock waves are well retrieved in the present first-order accurate computations.

5.1.3. Double shock-wave in pure liquid water

This test-case is very similar to the previous one but two shock-waves are now traveling to the left and to the right sides of the tube. The inner diameter of the pipe is here taken equal to $d = 19$ mm. The left part of the tube

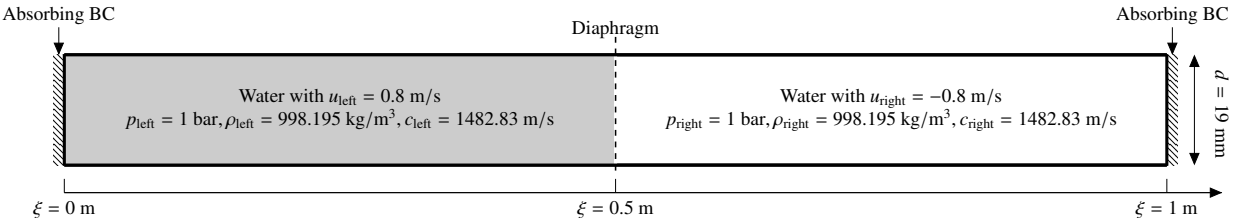

Figure 9: Test description of the double shock-wave problem in liquid water.

is initially filled with water with an initial velocity $u_{left} = 0.8$ m/s, an initial pressure of $p_{left} = 1$ bar, an initial density of $\rho_{left} = 998.195$ kg/m^3 and an initial speed of sound of $c_{left} = 1482.83$ m/s. The right part is initially filled with water with an initial velocity $u_{right} = -0.8$ m/s, an initial pressure of $p_{right} = 1$ bar, an initial density of $\rho_{right} = 998.195$ kg/m^3 and an initial speed of sound of $c_{right} = 1482.83$ m/s (see Fig. 9). Unlike the two previous shock-tube tests presented previously which are induced by a pressure jump between left and right states, this one is induced by a velocity jump. This corresponds to the abrupt closure of a valve at the end of a fluid-filled pipe. Temperature is supposed to be constant and set to 20°C in both sections of the tube.

Once again, the comparison between the present 1D/3D results with a Courant number of $C = 0.8$ (which corresponds to an averaged time step of $\Delta t \approx 1.35$ µs), the corresponding pure 1D results and the analytical solutions is discussed.The inlet and outlet of the pipe are modeled using absorbing (non-reflective) boundary conditions.

As in the previous case, the reference solution is obtained with the Joukowsky theory [47] based on the linearized low-Mach ($u_f \ll c_f$) and isothermal assumptions.

The profiles of pressure and velocity at $t_f = 0.2$ ms, measured as a function of the abscissa of the tube ($\xi \in [0\text{ m}, 1\text{ m}]$) are depicted in Fig. 10. The profiles obtained with the 1D/3D approach are compared to the analytical solution and to the 1D results. As previously, no discrepancy between the full 1D results and the 1D/3D results is observed. A good agreement between the numerical results and the analytical solution is also observed as the two shock-waves are correctly predicted.

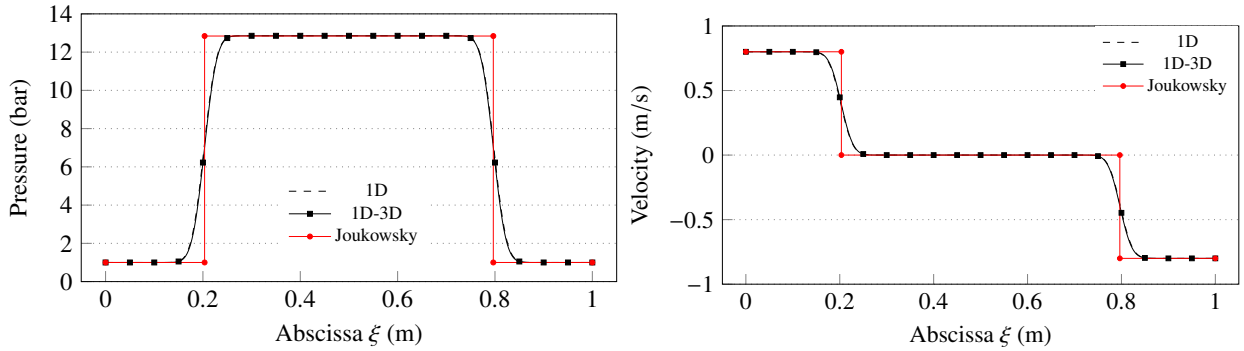

(a) (b)

Figure 10: Pressure (a) and velocity (b) profiles along the tube at $t_f = 0.2$ ms for the double shock-wave problem in liquid water: comparison between the 1D/3D results, the 1D results and the analytical solution.

For verification, the influence of the grid refinement has been also considered in order to underline the effect on the accuracy of the present numerical results. This verification has been performed on the three previous test-cases leading to the same conclusions. According to the numerical results obtained and not shown here for easy readability, the grid refinement of the pipe cross-section in the 3D regions has no influence on the accuracy of the present numerical results. It has to be noticed that in the case of very fine grids for the pipe cross-section, this can affect the value of the stable time step. In these specific cases, that means that the cells in the 3D regions have a high cell aspect ratio which is known to be avoided for both stability and accuracy reasons. What is more, the grid refinement in the axial direction has the same effect in pure 1D and in hybrid 1D/3D computations, i.e. more accurate results are obtained with finer meshes. Finally, the use of the ratio $\beta_{\mathcal{R}}$ in Eq. (4.2) makes it possible to obtain a similar behavior between 1D and 1D/3D computations for all pipe cross-section discretizations with moderate cell aspect ratios.

5.2. Bending beam problem

In order to assess the beam/shell Finite-Element coupling, a bending beam test problem is considered in this section. As can be seen on Fig. 11, a 1-m long beam is only subjected to its own weight ($g = 9.81\text{ m/s}^2$). The beam

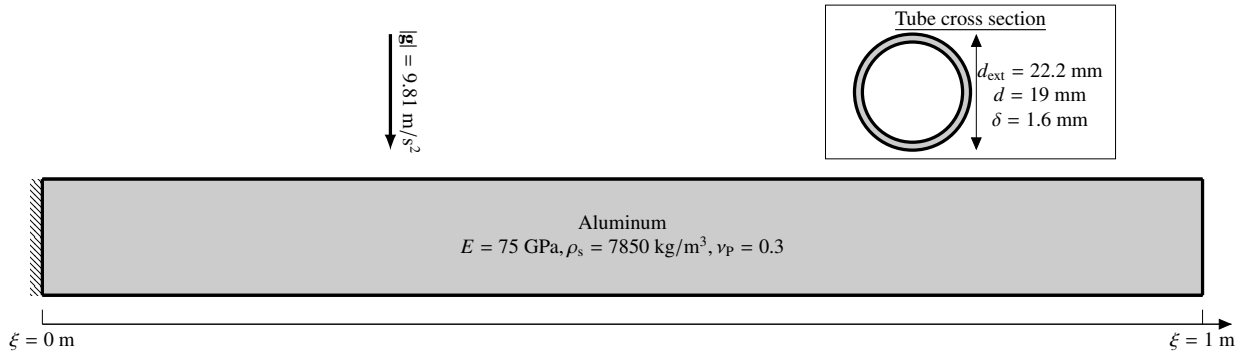

Figure 11: Test description of the beam bending problem.

is hollow and its section is circular with an internal diameter of $d = 19$ mm and a thickness of $\delta = 1.6$ mm which corresponds to an external diameter of $d_{\text{ext}} = 22.2$ mm. It corresponds to a section area of $A_s = 103.547$ mm^2 and to a moment of inertia of $I_s = \pi\left[(d+2\delta)^4 - d^4\right]/64 = 5525.78$ mm^4. The beam is made of aluminum with a Young modulus of $E = 75$ GPa, a density of $\rho_s = 7850$ kg/m^3 and a Poisson ratio of $\nu_P = 0.3$. The beam material is modeled using a standard linear elastic law. The left end of the pipe is clamped while the right end is free.

For the following hybrid 1D/3D computations, the tube is discretized using 1D beam elements from $\xi = 0$ m (which corresponds to the clamped end of the tube) to $\xi = 0.4$ m, then by 2D shell elements from $\xi = 0.4$ m to $\xi = 0.6$ m and finally by 1D beam elements from $\xi = 0.6$ m to $\xi = 1$ m (corresponding to the free end of the tube) as shown in Fig. 12.

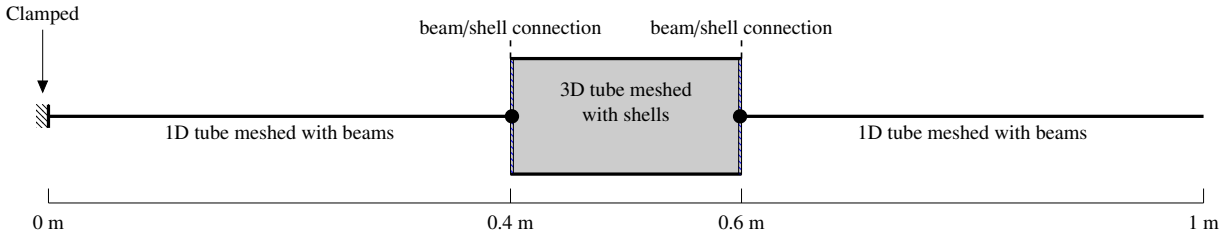

Figure 12: 1D/3D modeling of the beam bending problem.

The longitudinal length (in the $\boldsymbol{\xi}$ direction) of the cells corresponds to $h = 5$ mm. Furthermore, 16 shell elements are used for the discretization of the pipe cross-section circumference in the 3D regions. The 1D/3D mesh is thus composed of 158 beam elements in the 1D part of the computational domain and of 624 shell elements in the 3D region. The numerical results obtained with the 1D/3D numerical approach are then compared with the 1D results obtained with similar computational parameters (longitudinal length of cells and time step size). In addition, these numerical results are also compared with the analytical solution of the present problem derived from the Euler-Bernoulli beam theory.

5.2.1. Static analysis of coupled beam/shell elements

First, we study the steady-state deflection along the tube at rest. The analytical deflection d_ζ is given by:

$$d_\zeta(\xi) = \frac{-mg\xi^2}{24EI_sL}\left(\xi^2 - 4L\xi + 6L^2\right) \tag{5.1}$$

where ξ is the abscissa along the tube and $m = \rho_s A_s L = 0.812843$ kg is the total mass of the tube. To achieve a static response using explicit Finite-Element approaches, artificial damping is added to the model to suppress its transient response. In order to reach the steady state faster, a linear damping with a cut-off frequency is applied. In addition, the gravity loading is imposed linearly from $t = 0$ s to $t = 0.05$ s. The simulations are performed with a Courant number of $C = 0.8$ (which corresponds to an averaged time step of $\Delta t \approx 0.064$ µs). The computations are performed until the final time $t = 0.2$ s in order to obtain the steady-state solution. The results are shown in Fig. 13.

The full 1D results are perfectly superposed with the exact solution. The 1D/3D solution is in very good agreement with the exact solution but a small difference (< 1.8 % at the right) can be observed towards the end of the tube.

This can be explained by the fact that, in the 3D section, the assumption of the Euler-Bernoulli beam theory (on which the analytical solution is based) that beam plane sections remain plane is not valid anymore. In consequence, the 1D/3D result presents a slightly different deflection profile than the analytical and 1D results.

As previously, the influence of the grid refinement has been considered for verification. For this purpose, different computations have been performed with several successively refined meshes using the following grid size $h = 10$ mm, $h = 5$ mm and $h = 2.5$ mm. The corresponding numerical results not shown here for simplicity are similar demonstrating that the grid-independence is here reached.

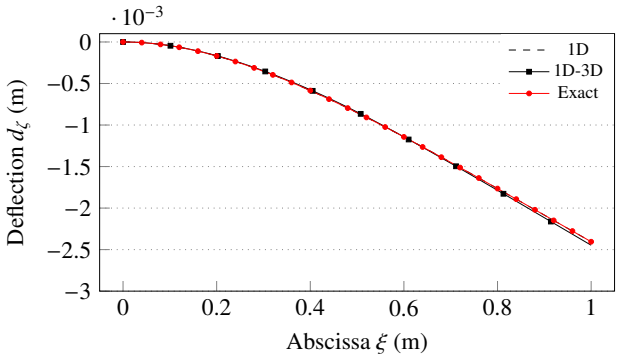

Figure 13: Deflection of the beam along the tube at rest : comparison between the 1D/3D results, the 1D results and the analytical solution.

5.2.2. *Dynamic analysis of coupled beam/shell elements*

Then, to make further comparison, the same cantilever beam is used for a dynamic analysis with zero damping. Without any kind of damping and subject to its own weight, the free end of the tube will oscillate at a known frequency and amplitude. Following [48], for the first mode, this frequency is given by:

$$f_1 = \frac{\alpha^2}{2\pi L^2}\sqrt{\frac{EI_s}{\rho_s A_s}} \tag{5.2}$$

with $\alpha = 1.875$ for a beam clamped at one end and free at the other end. In our case, $f_1 = 12.63$ Hz which corresponds to a period of $T_1 = 79.15$ ms. The amplitude is equal to two times the maximum deflection which is $D_{\max} = -4.81$ mm for the current case. The analytical solution of the deflection at the beam tip can be obtained by the Euler-Bernoulli beam theory leading to:

$$D(t) = -\frac{mgL^3}{8EI_s}\left[1 - \cos\left(\omega t\right)\right] \quad \text{with} \quad \omega = 2\pi f_1 \tag{5.3}$$

The results are shown in Fig. 14. Note that the gravity loading is imposed linearly from $t = 0$ s to $t = 0.02$ s, this is why the time axis only starts at $t = 0.02$ s.

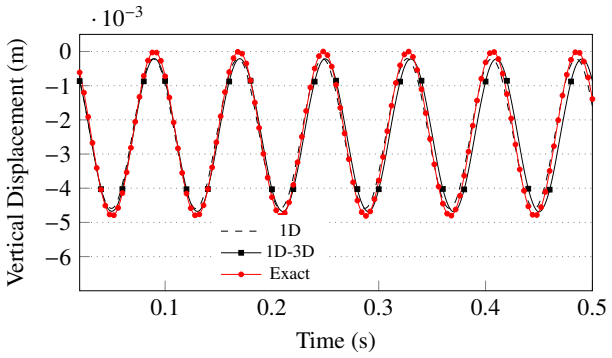

Figure 14: Displacement at the free end of the tube with time : comparison between the 1D/3D results, the 1D results and the analytical solution.

We observe an overall good agreement between the 1D result, the 1D/3D result and the analytical solution. For the current mesh resolution, both the 1D and 1D/3D are slightly underestimating the correct amplitude by less than 4.5 %. In addition, in the 1D/3D result, a time delay with the reference solution slightly grows with time. This can again been explained by the fact that Euler-Bernoulli beam theory (on which the analytical solution is based) assumptions are not respected in the 3D section. In consequence, the wave frequency is altered in the 3D section and is not constant with time as expected by the theory.

5.3. Aquitaine pipe whipping experiment

The Aquitaine experiments are a series of tests that were performed in CEA at the Aquitaine facility [49]. In this paper, we consider the so-called *Test 44*. It consists in generating the whipping of a pressurized pipe until it impacts a rigid wall. The pipe includes an elbow which is subject to strong deformations during the experiment. These experiments were designed to study the mechanical consequences of a sudden breach opening (*Loss-Of-Coolant-Accident*) in the primary pipe segment. Experimental data are available concerning the pipe motion and the impact force magnitude during this severe transient. The objective is here to assess the present 1D/3D coupling involving both 1D/3D fluid coupling and beam/shell elements coupling.

The studied test facility depicted in Fig. 15 consists of a water-filled piping system composed from left to right by a vessel with a capacity of 0.25 m^3 connected to a 0.12 m-long horizontal clamped pipe connected to a 0.12 m-long horizontal flexible pipe, a 90-deg flexible elbow with a 0.13 m radius of curvature and then a 0.2 m-long vertical flexible pipe. The internal diameter of the pipe is d = 88.9 mm and its thickness is δ = 7.62 mm. This piping system

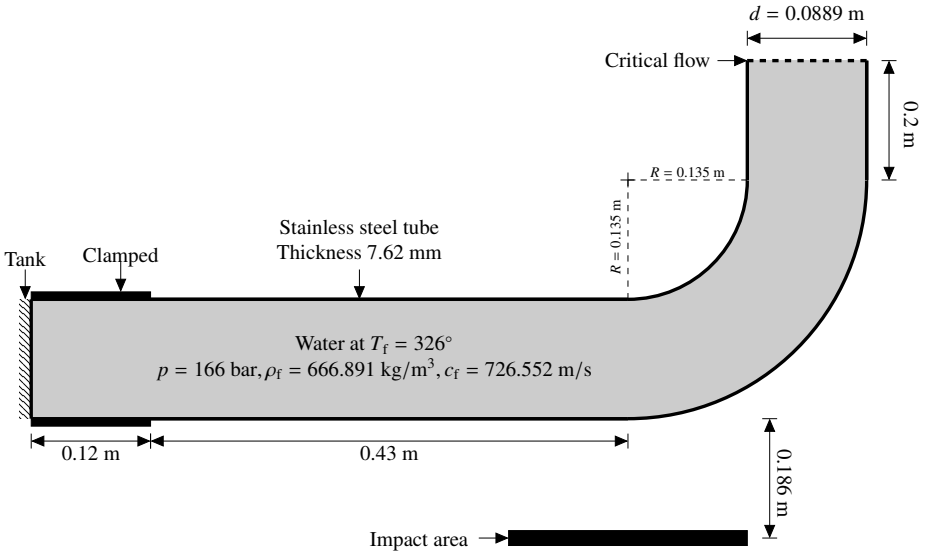

Figure 15: Test description of the Aquitaine pipe whipping experiments (1981) [50].

is filled by hot liquid water at rest with a pressure of p = 166 bar and a temperature of T_f = 326°C (which corresponds to the speed of sound c_f = 726.552 m/s). At the left side of the pipe, there is a tank and at the free end of the vertical pipe, there is a membrane that is assumed to break instantly at t = 0 ms. The flexible pipe mechanical behavior is modeled using a non linear elasto-plastic law with a von Mises criterion. Following [8, 40], the pipe material properties are as follows : Young's modulus E = 180 GPa, Poisson's ratio ν_P = 0.33, density ρ_s = 7800 kg/m^3, yield stress σ_y = 155 MPa, yield strain ϵ_y = 0.086 %, rupture limit stress σ_r = 475 MPa and deformation at rupture ϵ_r = 25 %. The steam-water flow is modeled using HEM in conjunction with the 1984 NBS/NRC Steam-Water Tables [19].

At t = 0 ms, the membrane breaks suddenly. The Moody model [51] is used to compute the critical flow at this boundary condition. At the inlet of the pipe, a specific boundary condition is used to represent the tank [7].

Moreover, on Fig. 16, the location of the different sensors is provided : point A corresponds to the junction between the horizontal rigid pipe and the horizontal flexible pipe, point E corresponds to the middle of the horizontal flexible pipe, point B corresponds to the beginning of the elbow and point C is located at the end of the elbow.

In the rigid part of the pipe (from the vessel to the end of the 0.12 m-long horizontal clamped pipe), only the fluid motion is modeled with a 1D FV approximation neglecting FSI effects. Then, the flexible part of the pipe is modeled by 1D coupled FV/FE elements in its straight horizontal section, then by 3D FV elements for the fluid coupled with 2D shell elements in the elbow section and finally by 1D coupled FV/FE elements in the final straight vertical section as shown in Fig. 16. The coupling between 1D and 3D domains are computed using the procedure described in

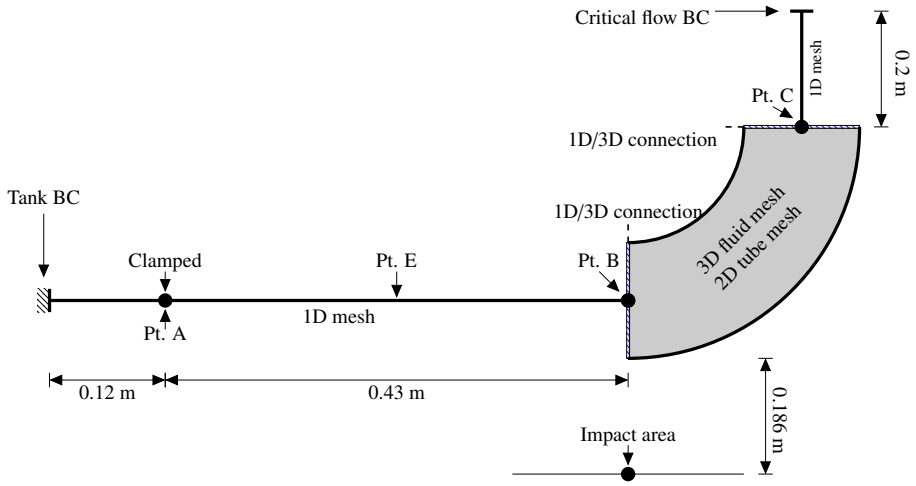

Figure 16: Model description of the 1D-3D Aquitaine test 44.

Sect. 4. In addition, the connection between the rigid and flexible pipes is performed using the junction treatment of several branches at the same location described in [7]. Moreover, the rezoning algorithm used to manage the fluid mesh motion in the 3D region is the same as the one previously considered in [40] such that, for each cross-section of the pipe elbow, the internal nodes of the fluid mesh follows via a homeomorphic motion the surface whose contour is defined by the Lagrangian nodes of the pipe circumference discretized using shell elements. The computation is performed with the Courant number $C = 0.5$ (which corresponds to an averaged time step of $\Delta t \approx 0.21$ µs). Second-order accurate computations are here considered for the fluid. This is achieved in the Finite-Volume approach with the MUSCL-Hancock method [30] as previously described in [31, 32].

The longitudinal length (in the $\boldsymbol{\xi}$ direction) of the cells corresponds to $h_{\text{tank-A}} = 4$ cm for the section that goes from the tank to Pt. A, $h_{\text{A-B}} = 3$ cm for the section that goes from Pt. A to Pt. B, $h_{\text{B-C}} = 2.82$ cm for the section that goes from the Pt. B to Pt. C, $h_{\text{C-end}} = 2.85$ cm for the section that goes from Pt. C to the outlet of the pipe. Furthermore, 48 cells are used for the discretization of the pipe cross-section in the 3D regions. Due to this discretization, the ratio between the pipe cross-section considered in the 1D domain and the discretized cross-section issued from the 3D region is about 1.0262. The 1D/3D mesh is thus composed of 158 cells in the 1D part of the computational domain and of 480 fluid cells and 160 shell elements in the 3D region.

The numerical results obtained are compared with the experimental data for test 44. In addition, the equivalent full 1D results issued from [8] are also shown to check the discrepancy between the full 1D results and the 1D/3D results. The global pipe motion is depicted in Fig. 17 showing the large vertical displacement of the piping system and the impacts of the elbow on the rigid obstacle leading to a local plastic crush of the pipe cross-section. Fig. 18 shows the elbow deformation induced by its impact on the rigid obstacle.

As observed in Fig. 19a, the pipe motion is well reproduced in the simulation. A higher vertical pipe displacement is obtained with the 1D/3D results compared to the full 1D approach because the pipe local crushing is not taken into account in full 1D. This is due to the reduced kinematics of the beam element, i.e. the variation of the cross-section is not considered. This was also observed in the previous study [40].

Next, the impact load is depicted in Fig. 19b. Due to the slight differences observed on the pipe displacement history, the impact time is not exactly the same between the full 1D, the hybrid 1D/3D numerical results and the experiments. In order to compare in a more precise way, the shape of the impact loading history, the impact times are set to be zero in Fig.19b for all of the numerical results and the experimental data. As seen in Fig. 19b, a very good agreement between the 1D/3D results and the experiment is obtained for the impact load. Compared to the full 1D result which strongly overestimates the impact load, the 1D/3D approach can reproduce the local crushing of the pipe and therefore returns a correct impact load. This clearly shows the interest of using models mixing 1D and 3D approaches where 3D modeling is used in the locations where the physics of interest requires a high level of detail.

In addition, the time history of the internal pressure is given at different locations along the pipe in Fig. 20: at the

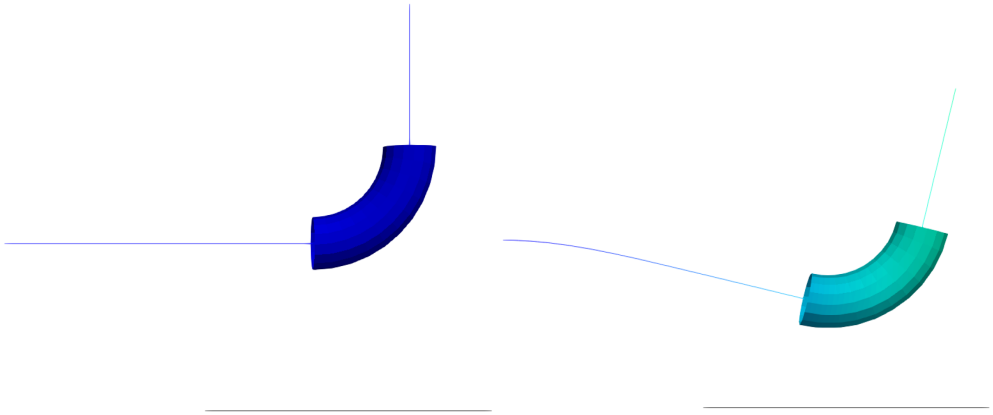

(a) t = 0 ms (b) t = 6.7 ms

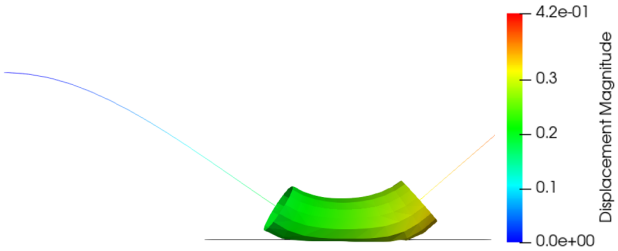

(c) t = 20 ms

Figure 17: Pipe motion during Aquitaine test 44 at selected instants during the simulation.

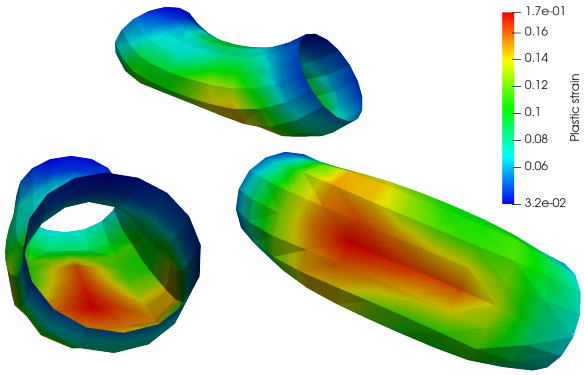

Figure 18: Different views of the plastic strain of the 3D section of the pipe after impact.

tank, at point A, at point E, at point B and at point C. It has to be noticed that the pressure in the tank decreases until the value of the saturation pressure.

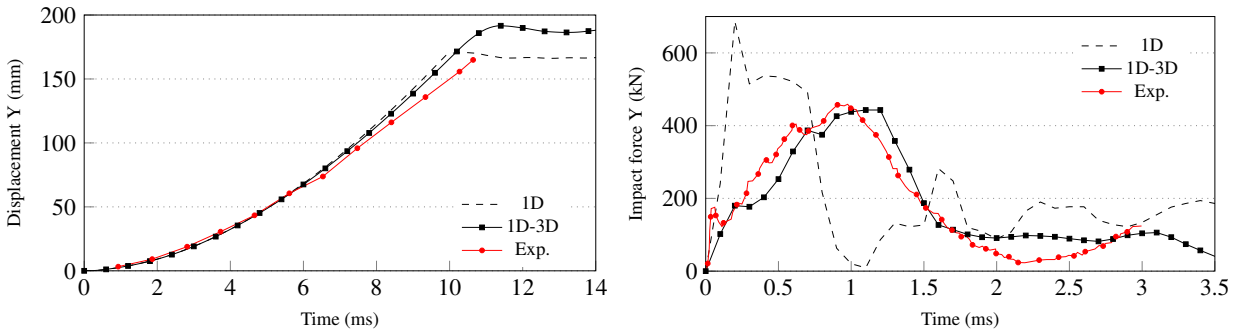

(a) Vertical displacement at Pt.B

(b) Impact force

Figure 19: Comparison between numerical results and experimental data for the Aquitaine test 44 issued from [50].

At every location except the tank, an important pressure surge can be observed at the moment of the impact (approximately from $t = 10$ ms to $t = 12$ ms) in the 1D/3D results. On the contrary, these pressure surges are absent from the full 1D results. This is due once again to the local crushing of the pipe which induces these pressure surges that is not taken into account in the full 1D simulations.

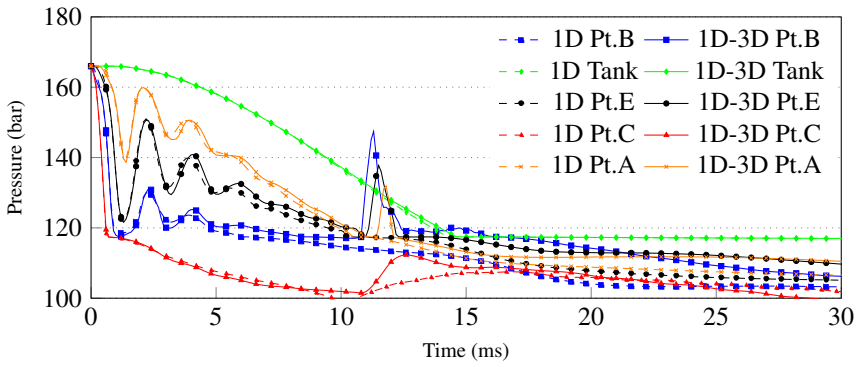

Figure 20: Pressure time history in the vessel and at different locations along the pipe for the Aquitaine test 44.

In order to give a more detailed insight on the behavior of the 1D/3D coupling (located at point B and point C), extra plots showing variables state evolution on both sides of the common 1D/3D interfaces (1D side vs 3D side).

In Fig. 21, the time evolutions of fluid-related variables (pressure, velocity and void fraction) on both sides of the 1D/3D interfaces are depicted. One can see that these variables are very slightly affected by the present coupling which confirms that its presence does not affect variables that are expected to be conserved through the interface between 1D and 3D computational domains even in moving frames.

In Fig. 22, the time evolution of von Mises stresses (from beam and shell finite elements) in the tube on both sides of the 1D/3D interfaces are shown. For the 3D part, the von Mises stresses on elements located in the internal and external part of the elbow are presented. It can be observed that the von Mises are of the same order of magnitude in the 1D and 3D domain until impact ($t = 10$ ms). After impact, differences are growing since the local crushing of the pipe is not taken into account in 1D.

In Fig. 23, the plastic strains evolution with time are shown. First, one can see that, in the 3D section, the inner part of the elbow suffers less plastic deformation than the outer part which is expected as the impact happens on the outer part. Then, it appears clearly that plastic strains are underestimated in the 1D part compared to the 3D part. It is justified because, in 1D, the tube is not crushed by the whipping against the wall which leads to smaller strains

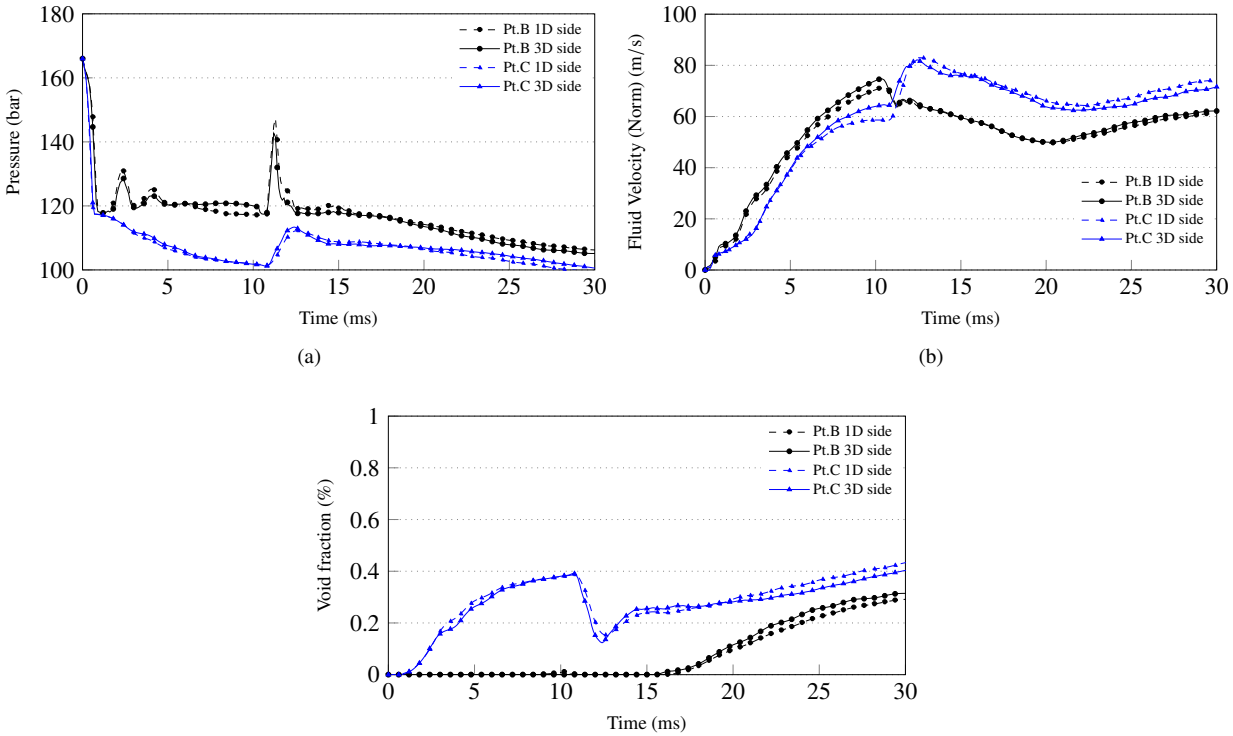

Figure 21: Pressure (a), velocity (b) and void fraction (c) time evolution at the 1D/3D interfaces.

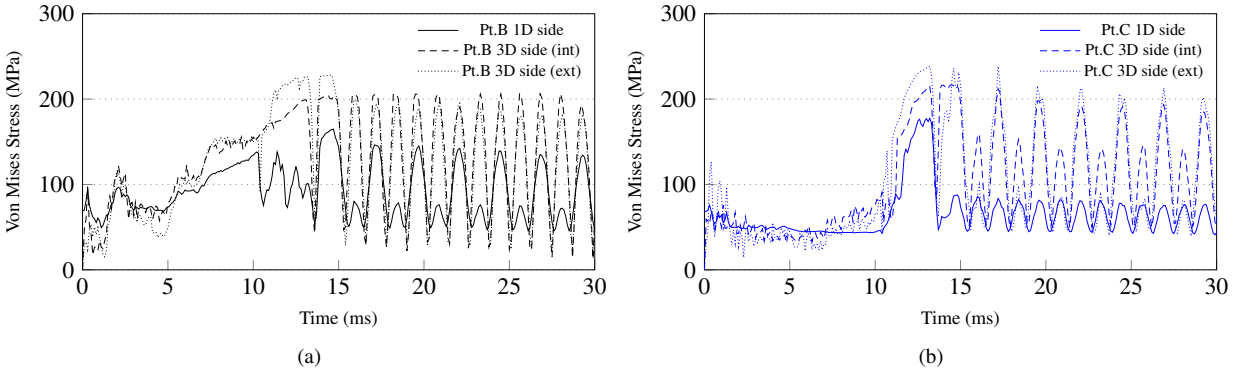

Figure 22: Time evolution of the von Mises stress at the 1D/3D interfaces.

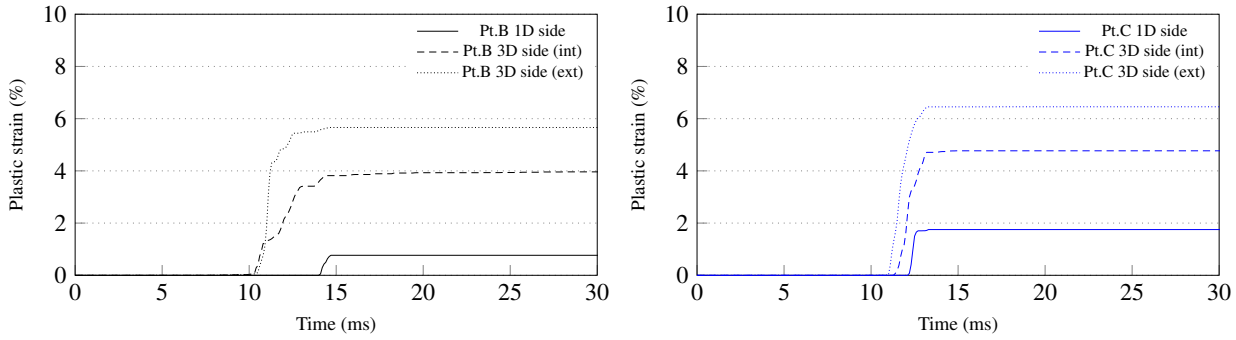

(a) (b)

Figure 23: Time evolution of the plastic strain at the 1D/3D interfaces.

compared to the 3D section.

In addition, the influence of the mesh refinement in the pipe direction as well as the one of the pipe cross-section on the present numerical results have been studied. For this purpose, the Aquitaine pipe whipping computations have been performed using different grid size. Five numerical results are compared in Fig. 24 showing the effect

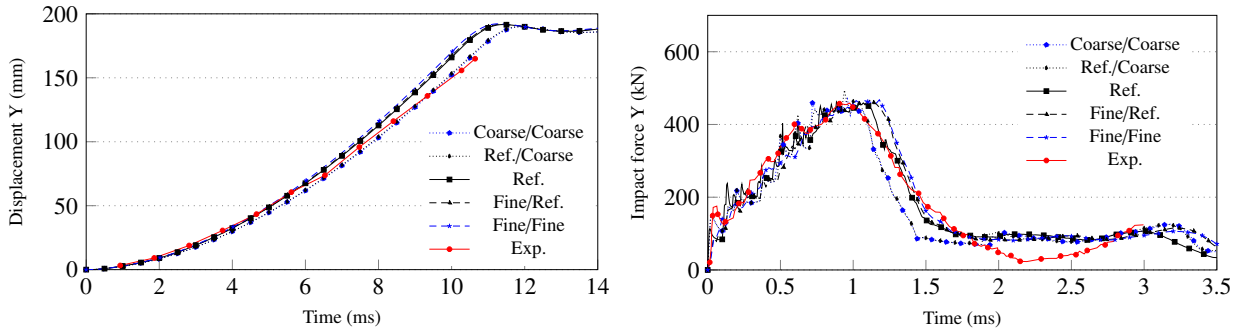

(a) Vertical displacement at Pt.B (b) Impact force

Figure 24: Influence of the mesh refinement for the 1D/3D computations of the Aquitaine pipe whipping experiments (test 44).

of the mesh refinement on the vertical pipe displacement and on the impact load. The numerical results considered previously are labelled "Ref." whereas the numerical solution labelled "Ref./Coarse" is obtained using the same discretization in the pipe direction and twice less points for the pipe cross-section in comparison with the reference computation. The numerical results labelled "Coarse/Coarse" are obtained with twice less points in the pipe direction and in the pipe cross-section compared to the mesh used for the initial computation. On the contrary, the numerical results obtained with twice more points in the pipe direction in conjunction with the *reference* pipe cross-section are labelled "Fine/Ref." while the ones labelled "Fine/Fine" consider twice more points in the two discretizations in comparison with the "Ref." computation. The agreement between the numerical results obtained with the two finest grids and the reference one observed on Fig. 24 shows that the grid-independence of the numerical solution is reached. In addition, it seems that with the two coarsest grids, the pipe exhibits a stiffer behavior than observed in the other computations. This is observed in Fig. 24b showing that the impact force pic is shorter with the two less refined grids. Nevertheless, in all of the considered 1D/3D computations, a good agreement with the experimental data are observed.

Finally, a full 3D FSI modeling of the Aquitaine pipe whipping experiment have been also considered here. In this 3D modeling, the flexible part of the pipe which is 0.52-m long is modeled in 3D whereas the rigid part of the pipe

is still modeled in 1D for simplicity. The numerical results not shown here for easy readability are in agreement with their 1D/3D counterpart. However, using the 1D/3D hybrid approach makes it possible to reduce the computational cost by a factor of 2.6 in comparison with the 3D computation. This factor corresponds to the ratio of the pipe lengths modeled in 3D between the two computations: 0.52 m for the full 3D computation versus 0.2 m for the 1D/3D one. Note that in realistic industrial cases where long and complex networks of pipelines are considered, computational savings obtained with the present 1D/3D approach can be significant as the size of the 3D domain including in the computational domain is small in comparison to the global length of the considered network.

6. Conclusion and perspective

In this paper, a procedure to couple 1D and 3D FSI models is presented in a mixed Finite-Volume/Finite-Element framework for the simulation of fast-transient phenomena in pipelines. The considered FSI models are based on the Euler/Homogeneous Equilibrium Model equations in interaction with Euler-Bernoulli beam elements for 1D models or with shell elements for 3D models. The proposed 1D/3D fluid Finite-Volume coupling is built upon the preservation of the numerical fluxes between the 1D and the 3D fluid computational domains such as the conservation of mass, momentum and total energy is accounted for. These numerical fluxes are obtained via the numerical approximation of the local Riemann problems at the cell faces constituting the common 1D/3D interface. Furthermore, the present 1D/3D coupling makes it possible to deal with general Equations Of State. In addition, the proposed 1D/3D fluid coupling is associated with a beam/shell elements coupling for the mechanical pipe behavior. For this purpose, constraint conditions based on geometric considerations are applied in order to impose relationships between the degrees of freedom of beam and shell elements at the nodes of the common interface. The present 1D/3D coupling approach makes thus it possible to insert 3D regions at the locations where the physical phenomena of interest require a high degree of resolution. This is thus very useful to overcome the inherent 1D modeling limitations while keeping a reasonable execution time. Finally, the proposed 1D/3D coupling is assessed on a selection of analytical and experimental test cases (purely fluid shock-tubes in both air and water, purely structural bending beam problem and a coupled FSI pipe whipping experiment) showing its efficiency and accuracy. In particular, complex wave propagation phenomena are well captured and pipe deformations can also be retrieved thanks to the use of shell elements.

The present 1D/3D coupling approach is based on the conservation of the flow variables, i.e. mass, momentum and energy, at the common interface. Further investigation will be done to assess the global energy balance between fluid and structure. In the present 1D/3D coupling approach, the kinematics of the shell elements has to follow the reduced kinematics of the beam element at the common interface. As a consequence, the pipe cross-section is assumed to be rigid and constant in time. However, in fast-transient phenomena in piping systems, the variations of the pipe cross-section induced by the fluid internal pressure changes due to the pipe wall elasticity are known to affect the pressure wave speeds and amplitudes. A beam/shell elements coupling taking into account this phenomena will thus be considered in the future. In addition, the extension of the present 1D/3D fluid coupling to compressible two-phase flow models involving both conservative and non-conservative terms such as the Baer-Nunziato model will also be considered in the future.

Acknowledgments

This work has been achieved within the framework of the “FAST” project of the EDF/CEA/Framatome tripartite Institute. Computational facilities were provided by EDF. Numerical simulations have been performed with the *Europlexus* software [41] (`http://www-epx.cea.fr/`).

References

[1] S. Li, B. W. Karney, G. Liu, FSI research in pipeline systems A review of the literature, J. Fluids Struct. 57 (2015) 277–297.
[2] A. Bergant, A. R. Simpson, A. S. Tijsseling, Water hammer with column separation: A historical review, J. Fluids Struct. 22 (2) (2006) 135–171.
[3] D. C. Wiggert, Fluid transients and fluid-structure interaction in flexible liquid-filled piping, ASME Pressure Vessels and Piping Conference, Chicago, USA (1986) (1986).
[4] A. S. Tijsseling, Fluid-structure interaction in liquid-filled pipe systems: A review, J. Fluids Struct. 10 (1996) 395–420.

[5] D. C. Wiggert, A. S. Tijsseling, Fluid transients and fluidstructure interaction in flexible liquid-filled piping, ASME Appl. Mech. Rev. 54 (2001) 455–481.
[6] D. Ferras, P. Manso, A. J. Schleiss, D. Covas, One-dimension fluid-structure interaction models in pressurized fluid-filled pipes: a review, Appl. Sci. 8 (2018) 1–33.
[7] F. Daude, P. Galon, A Finite-Volume approach for compressible single- and two-phase flows in flexible pipelines with fluid-structure interaction, J. Comput. Phys. 362 (C) (2018) 375–408.
[8] F. Daude, P. Galon, Ch. 7.e. Reactor Pipelines, in: A. Shams (Ed.), Computational Fluid-Structure Interaction for Nuclear Reactor Applications, Elsevier (In Revision), 2020, pp. 1–32.
[9] R. F. Kulak, Three-dimensional fluid-structure coupling in transient analysis, Comput. Struct. 21 (1985) 529–542.
[10] M. J. Castro, P. G. Le Floch, M. L. Muñoz Ruiz, C. Parés, Why many theories of shock waves are necessary: Convergence error in formally path-consistent schemes, J. Comput. Phys. 227 (17) (2008) 8107–8129.
[11] R. Abgrall, S. Karni, A comment on the computation of non-conservative products, J. Comput. Phys. 229 (8) (2010) 2759–2763.
[12] J.-M. Hérard, O. Hurisse, Coupling two and one-dimensional unsteady Euler equations through a thin interface, Comput. Fluids 36 (2007) 651–666.
[13] M. Deininger, U. Iben, C.-D. Munz, Coupling of three- and one-dimensional hydraulic flow simulations, Comput. Fluids 190 (2019) 128–138.
[14] C. Wang, H. Nilsson, J. Yang, O. Petit, 1D-3D coupling for hydraulic system transient simulations, Comput. Phys. Commun. 210 (2017) 1–9.
[15] G. Montenegro, A. Onorati, A. Della Torre, The prediction of silencer acoustical performances by 1D, 1D-3D and quasi-3D non-linear approaches, Comput. Fluids 71 (2013) 208–223.
[16] F. Bellamoli, L. O. Müller, E. F. Toro, A numerical method for junctions in networks of shallow-water channels, Appl. Math. Comput. 337 (2018) 190–213.
[17] R. J. Ho, S. A. Meguid, Z. H. Zhu, R. G. Sauvé, Consistent element coupling in nonlinear static and dynamic analyses using explicit solvers, Int. J. Mech. Mater. Des. 6 (2010) 319–330.
[18] F. Casadei, J. P. Halleux, An algorithm for permanent fluid-structure interaction in explicit transient dynamics, Comput. Methods Appl. Mech. Engrg. 128 (24-25) (1995) 231–289.
[19] L. Haar, J. S. Gallangher, G. S. Kell, NBS/NRC Steam Tables: Thermodynamic and Transport Properties and Computer Programs for Vapor and Liquid States of Water in SI Units, Hemisphere Publishing Co., 1984.
[20] F. Daude, A. S. Tijsseling, P. Galon, Numerical investigations of water-hammer with column-separation induced by vaporous cavitation using a one-dimensional Finite-Volume approach, J. Fluids Struct. 83 (2018) 91–118.
[21] F. Daude, P. Galon, Simulations of single- and two-phase shock tubes across abrupt changes of area and branched junctions, Nuclear Eng. Design 365 (C) (2020) 110734.
[22] C. W. Hirt, A. A. Amsden, J. L. Cook, An Arbitrary Lagrangian-Eulerian Computing Method for All Flow Speeds, J. Comput. Phys. 14 (3) (1974) 227–253.
[23] P. D. Thomas, C. K. Lombard, Geometric conservation law and its application to flow computations on moving grids, AIAA J. 17 (10) (1979) 1030–1037.
[24] C. Farhat, P. Geuzaine, C. Grandmont, The discrete geometric conservation law and the nonlinear stability of ALE schemes for the solution of flow problems on moving grids, J. Comput. Phys. 174 (2) (2001) 669–694.
[25] E. F. Toro, M. Spruce, W. Speares, Restoration of the contact surface in the HLL-Riemann solver, Shock Waves 4 (1) (1994) 25–34.
[26] E. F. Toro, Riemann Solvers and Numerical Methods for Fluid Dynamics. A Practical Introduction, 3d edition, Springer, 2009.
[27] E. F. Toro, The HLLC Riemann solver, Shock Waves 4 (1) (2019) 25–34.
[28] H. Luo, J. D. Baum, R. Lohner, On the computation of multi-material flows using ALE formulation, J. Comput. Phys. 194 (1) (2004) 304–328.
[29] P. Batten, N. Clarke, C. Lambert, D. M. Causon, On the choice of wavespeeds for the HLLC Riemann solver, SIAM J. Sci. Comput. 18 (6) (1997) 1553–1570.
[30] B. van Leer, On the relation between the upwind-differencing schemes of Godunov, Engquist-Osher and Roe, SIAM J. Scientific Statist. Comput. 5 (1) (1984) 1–20.
[31] F. Daude, P. Galon, Z. Gao, E. Blaud, Numerical experiments using a HLLC-type scheme with ALE formulation for compressible two-phase flows five-equation models with phase transition, Comput. Fluids 94 (1) (2014) 112–138.
[32] D. Iampietro, F. Daude, P. Galon, A low-diffusion self-adaptive flux-vector splitting approach for compressible flows, Comput. Fluids 206 (C) (2020) 104586.
[33] M. Lesoinne, C. Farhat, Geometric conservation laws for flow problems with moving boundaries and deformable meshes, and their impact on aeroelastic computations, Comput. Methods Appl. Mech. Engrg. 134 (1-2) (1996) 71–90.
[34] P. Geuzaine, C. Grandmont, C. Farhat, Design and analysis of ALE schemes for provable second-order time-accuracy for inviscid and viscous flow simulations, J. Comput. Phys. 191 (1) (2003) 206–227.
[35] H. Zhang, M. Reggio, J. Y. Trépanier, R. Camarero, Discrete form of the GCL for moving meshes and its implementation in CFD schemes, Comput. Fluids 22 (1) (1993) 9–23.
[36] B. Nkonga, H. Guillard, Godunov type method on non-structured meshes for three-dimensional moving boundary problems, Comput. Methods Appl. Mech. Engrg. 113 (1-2) (1994) 183–204.
[37] H. Guillard, C. Farhat, On the significance of the geometric conservation law for flow computations on moving meshes, Comput. Methods Appl. Mech. Engrg. 190 (11-12) (2000) 1467–1482.
[38] C. Farhat, M. Lesoinne, Two efficient staggered algorithms for the serial and parallel solution of three-dimensional nonlinear transient aeroelastic problems, Comput. Methods Appl. Mech. Engrg. 182 (3-4) (2000) 499–515.
[39] S. Giuliani, An algorithm for continuous rezoning of the hydrodynamic grid in Arbitrary Lagrangian-Eulerian computer codes, Nuclear Eng. Design 72 (2) (1982) 205–212.
[40] S. Potapov, P. Galon, Modelling of Aquitaine II pipe whipping test with the *Europlexus* fast dynamics code, Nuclear Eng. Design 235 (17-19) (2005) 2045–2054.
[41] Joint Research Centre (JRC), Commissariat à l'énergie atomique et aux énergies alternatives (CEA), *Europlexus* user's manual,

http://europlexus.jrc.ec.europa.eu/ (2020).
[42] T. Belytschko, W. K. Liu, B. Moran, K. I. Elkhodary, Nonlinear Finite Elements for Continua and Structures, 2d edition, Wiley, 2014.
[43] F. Casadei, N. Leconte, Coupling finite elements and finite volumes by Lagrange multipliers for explicit dynamic fluid-structure interaction, Int. J. Numer. Meth. Eng. 86 (1) (2011) 1–17.
[44] S. R. Wu, L. Gu, Introduction to the Explicit Finite Element Method for Nonlinear Transient Dynamics, Wiley, 2012.
[45] S. W. Key, Transient response by time integrations: review of implicit and explicit operators, in: J. Donea (Ed.), Advanced Structural Dynamics, Applied Science Publishers, UK, 1980, pp. 71–95.
[46] V. Aune, G. Valsamos, F. Casadei, M. Larcher, M. Langseth, T. Børvik, Use of damage-based mesh adaptivity to predict ductile failure in blast-loaded aluminium plates, Proc. Eng. 197 (2017) 3–12.
[47] N. Joukowsky, Über den hydraulischen Stoss in Wasserleitungsröhren (On the hydraulic hammer in water supply pipes), Mémoires de l'Académie Impériale des Sciences de St.-Pétersbourg 9(5) (1898) 1–71, (in German).
[48] R. D. Blevins, Natural frequency of beams, in: Formulas for Dynamics, Acoustics and Vibration, John Wiley & Sons, Ltd, 2016, pp. 134–202.
[49] J. L. Garcia, P. Chouard, E. Sermet, Experimental studies of pipe impact on rigid restraints and concrete slabs, Nuclear Eng. Design 77 (1984) 357–368.
[50] J. L. Garcia, "AQUITAINE 2 - Interprétation" Analyse d'essais de fouettements de tuyauteries avec chocs sur structures rigides, Tech. Rep. DRE/STRE/LMA/81-373, CEA (1981).
[51] F. J. Moody, Maximum flow rate of a single component two-phase mixture, ASME J. Heat Transfer 87 (1965) 134–141.